

The Rotational and Spin-Rotational Level Structure of para- H_2^+ from High-Resolution MQDT-Assisted Rydberg-State Spectroscopy

I. Doran

Department of Chemistry and Applied Biosciences, ETH Zürich, Zürich, Switzerland

M. Beyer

*Department of Physics and Astronomy, LaserLaB, Vrije Universiteit Amsterdam,
de Boelelaan 1081, 1081 HV Amsterdam, The Netherlands*

F. Merkt*

Department of Chemistry and Applied Biosciences, ETH Zürich, Zürich, Switzerland

Department of Physics, ETH Zürich, Zürich, Switzerland and

Quantum Center, ETH Zürich, Zürich, Switzerland

(Dated: November 6, 2024)

The structure of the low-lying rotational levels of the $X^+ \ ^2\Sigma_g^+$ ($v^+ = 0$) vibronic ground state of para- H_2^+ has been determined by combining frequency-comb calibrated continuous-wave high-resolution laser spectroscopy of nf Rydberg series in the range of principal quantum number n between 28 and 115 and Rydberg-series extrapolation using multichannel-quantum-defect theory (MQDT). The use of accurate quantum-defect parameters obtained from new ab initio calculations enabled the experimental determination of the pure rotational term values of the $N^+ = 2, 4$ and 6 rotational levels of H_2^+ with sub-MHz accuracy (174.236 744 6(77), 575.455 632 5(86) and 1191.385 571(240) cm^{-1} , respectively), and of the corresponding spin-rotational coupling constants with an accuracy of better than 100 kHz (42.21(4), 41.26(8) and 40.04(8) MHz, respectively). These values are in agreement with the results of first-principles calculations that include high-order relativistic and quantum-electrodynamics corrections to the level energies. To reach the reported accuracy in the Rydberg series extrapolation, it was necessary to correct for artificial level shifts arising in the MQDT calculations in the vicinity of local perturbations of high- n Rydberg states with a $v^+ = 0$ H_2^+ ion core caused by low- n core-excited Rydberg states, and resulting from approximations in the treatment of the Rydberg-electron energy in the interacting channels.

I. INTRODUCTION

Molecular hydrogen, in its neutral (H_2) and ionized (H_2^+) forms and their deuterated isotopomers $\text{HD}^{(+)}$ and $\text{D}_2^{(+)}$, is a fundamental molecular system, with which physical theories and models can be tested by comparison of experiment and theory. First-principles quantum-mechanical calculations treating relativistic and quantum-electrodynamics (QED) effects perturbatively to high orders in the fine-structure constant α provide extremely precise predictions of the level structures, at the level of about 300 kHz and about 1 kHz for the rovibrational levels of the electronic ground state of H_2 [1, 2] and H_2^+ [3–10], respectively. Calculations of the hyperfine structure of these ions have also been performed with high accuracy [5, 8, 10]. In recent years, the validity of these calculations has been confirmed experimentally with increasing precision, reaching the level where comparison between theory and experiment helps improving the values of the fundamental constants (e.g., α and the Rydberg constant R_∞) and particle properties (e.g., magnetic moments, nuclear radii, and nuclear-to-electron mass ratios) used as parameters, and even searching for

physics beyond the standard model of particle physics [9, 11–18].

H_2 and H_2^+ also play an important role in studies of primary photo-chemical and -physical processes such as photoionization and photodissociation, but the excited molecular states that are typically involved in these processes cannot currently be calculated as precisely as the electronic ground state. The level structures of H_2 and H_2^+ are linked through the process of photoionization and this link is elegantly exploited by multichannel quantum-defect theory (MQDT) [19–24] to relate the neutral and ionized forms of a molecule through the concept of ionization channels. An ionization channel includes the ionization continuum (e.g., $\text{H}_2^+(\alpha^+) + e^-(\epsilon, \ell)$ in the case of H_2) associated with a given quantum state α^+ of the ionized species and with a photoelectron partial wave of orbital angular momentum quantum number ℓ at energy ϵ in the continuum, and the infinite series $n\ell[\alpha^+]$ of Rydberg states with principal quantum number n converging on the $\text{H}_2^+(\alpha^+) + e^-(\epsilon = 0)$ threshold [22, 24, 25]. As $n \rightarrow \infty$, the discrete level structure of the neutral molecule approaches that of the ionized molecule and there is therefore no fundamental reason why calculations of electronically highly excited states of neutral molecules could not reach the accuracy achievable for the ionized species. Standard ab initio quantum-chemical methods fail in this respect because of the rapidly increasing size

* frederic.merkt@phys.chem.ethz.ch (F. Merkt)

of the basis sets required to reach convergence. In contrast, MQDT, which treats the ionization channels and their interactions as electron-ion collisions in the framework of collision theory, becomes increasingly accurate as n increases because the description of the channels as consisting of an electron and an ion core becomes more and more realistic.

This convergence enables the determination of the level structure of the ionized species through measurements of Rydberg spectra at high n values. The first experimental determination of the rovibrational level structure of H_2^+ in its $X^+ \ ^2\Sigma_g^+$ electronic ground state was indeed through measurements of high Rydberg states of H_2 and extrapolation using early forms of MQDT [21]. Over the years, MQDT has been systematically refined and extended (see, e.g., Refs. [22, 24, 26–40]) and can be used today to determine the level structure of ionized molecules with an accuracy limited by the bandwidth of the radiation used to record Rydberg spectra, or the natural linewidth or Doppler broadening [36, 41–43]. Even more importantly, MQDT can also be used to study molecular photoionization and characterize the structure and dynamics of highly excited electronic states of neutral molecules.

In the present article, we report on a systematic investigation, by high-resolution laser spectroscopy and over a broad range of n values, of the nf Rydberg series converging to the lowest rotational states (N^+ up to 6) of the ground vibronic state of para- H_2^+ . The purpose of this investigation was threefold. Firstly, it aimed at testing a new set of purely ab initio quantum defect parameters extracted from recent high-level electronic-structure calculations of low- n Rydberg states [44–47] by comparing the results of full MQDT calculations with those obtained by high-resolution spectroscopy. In the course of this study, we observed, with full spectroscopic detail, a limitation of the currently implemented fully ab initio MQDT formalism arising from the ambiguity in the definition of the Rydberg-electron energy in spectral regions where Rydberg series are strongly perturbed by channel interactions [24, 48–50]. We demonstrate how the systematic errors originating from this ambiguity can be strongly suppressed using an empirical two-channel correction model.

Secondly, it aimed at providing a full understanding of the phenomena accompanying the uncoupling of the Rydberg electron from the ion arising at increasing n value. The level structure evolves from a situation, at low- n values, where the Rydberg and core electrons are coupled through the electrostatic exchange interaction and have a well-defined total electron spin to a situation, at high n values, where the core electron is coupled to the ion-core rotation and the Rydberg states have fully mixed singlet and triplet character. Series converging to even N^+ rotational levels were selected to specifically investigate the effects of the spin-rotation fine structure of the ion core, which are masked in ortho- H_2^+ by the much stronger uncoupling effects caused by the hyperfine in-

teraction [36]. A first analysis of this uncoupling phenomenon by MQDT was reported in an investigation of the $nfN^+ = 2$ series of para- H_2 by THz spectroscopy from nd levels [51]. This previous study led to the determination of the interval between the lowest two rotational levels of para- H_2^+ with an accuracy of 2.3 MHz, limited by the bandwidth of the pulsed laser THz radiation used in the experiments. The spectral resolution was, however, not sufficient to fully resolve the fine structure of the Rydberg series so that the spin-rotation interval of the $N^+ = 2$ ionic level could not be determined. The possibility to resolve the fine structure of the $nfN^+ = 2$ series and to determine the spin-rotational interval of the $N^+ = 2$ ionic level was later demonstrated in the thesis of Beyer [52]. In the present work, the use of frequency-comb-calibrated continuous-wave single-mode laser radiation enabled a significant improvement of the precision and accuracy of the measurements and the recording of fully resolved fine-structure patterns over a broad range of principal quantum numbers for the $nfN^+ = 2, 4$ and 6 Rydberg series.

Finally, our study aimed at determining the rotational and spin-rotational structure in the ground vibronic state of para- H_2^+ by combining precision Rydberg spectroscopy and MQDT, focusing on the spin-rotation fine structure that could not be determined in Ref. [51]. H_2^+ does not have electric-dipole-allowed rovibrational transitions and Rydberg-series extrapolation is an attractive approach to determining its level structure. While spin-rotation intervals in higher vibrational levels of H_2^+ have been measured very precisely (precision in the kHz range) by Jefferts [53] with magnetic dipole transitions, no experimental values for the spin-rotation intervals in the ground vibronic state have been reported to date.

In the para- H_2^+ ion core, the spin-rotation interaction leads to splittings of the ionic energy levels (see panel (b) of Fig. 1)

$$\Delta E_{\text{SR}}(N^+) = hc\gamma_{\text{SR}}^{N^+} \left(N^+ + \frac{1}{2}\right), \quad (1)$$

that rapidly increase with the rotational quantum number N^+ of the ion core. In Equation (1), $\gamma_{\text{SR}}^{N^+}$ is the N^+ -dependent spin-rotation coupling constant which, at low N^+ values, can be well described by retaining only the first-order centrifugal-distortion contribution (see, e.g., Refs. [54, 55]):

$$\gamma_{\text{SR}}^{N^+} = \gamma^{(0)} + \gamma^{(1)}N^+(N^+ + 1). \quad (2)$$

The spin-rotation interaction in the ion core also significantly affects the fine structure of high- n Rydberg states and is the driving force, in para- H_2 , of the uncoupling of the Rydberg electron as n increases, as explained above.

Fig. 1 illustrates the principle of our measurements. Transitions to Rydberg states belonging to series converging to the $v^+ = 0, N^+ = 2, 4$ and 6 levels of the $X^+ \ ^2\Sigma_g^+$ state of H_2^+ are measured from the GK $^1\Sigma_g^+(v = 0, N = 0, 2)$ and $\text{I}^+ \ ^1\Pi_g^+(v = 0, N = 4)$ intermediate states of H_2 , which are themselves populated

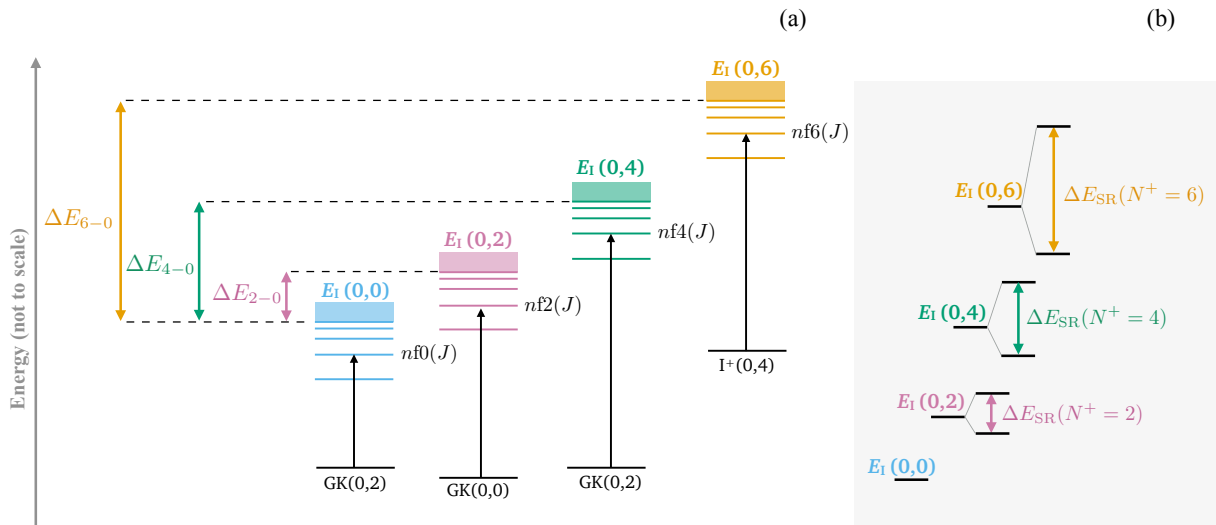
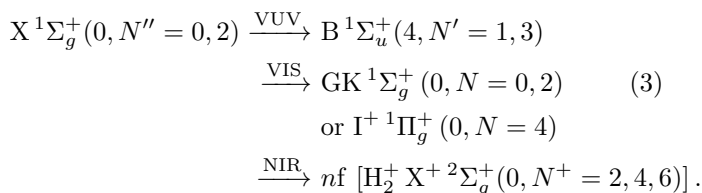


Figure 1. (a) Schematic energy-level diagram (not to scale) showing the transitions to nf Rydberg states of para- H_2 used to determine the ΔE_{2-0} , ΔE_{4-0} , and ΔE_{6-0} rotational intervals of the $X^+ \ ^2\Sigma_g^+(v^+ = 0)$ ground state of para- H_2^+ by Rydberg series extrapolation. (b) Detailed view (not to scale) including the spin-rotation splittings of the $N^+ = 0, 2, 4$ and 6 levels of H_2^+ .

from the $X \ ^1\Sigma_g^+(v = 0, N = 0, 2)$ state by resonant two-photon excitation via the $B \ ^1\Sigma_u^+(v = 4, N = 1, 3)$ states. The resonant nature of the excitation scheme enables a clean selection of para- H_2 and avoids the generation of ions by multiphoton ionization. In the remainder of this article, the Rydberg states are labeled $n\ell N^+(J)$, where n is the principal quantum number, ℓ is the quantum number associated with the orbital angular momentum of the Rydberg electron, N^+ is the rotational angular momentum quantum number of the ion core, and J is the quantum number for the total angular momentum in para- H_2 (total nuclear spin $I = 0$).

II. EXPERIMENTAL PROCEDURE

The Rydberg states are accessed using the resonant three-photon excitation sequence



Rydberg states converging to the $N^+ = 2$ and $N^+ = 4$ rotational levels of H_2^+ are excited from the $X \ ^1\Sigma_g^+(0, 0)$ ground state via the $B \ ^1\Sigma_u^+(4, 1)$ and $\text{GK} \ ^1\Sigma_g^+(0, 0)$ ($\tau \approx 79$ ns [56]) intermediate states and via the $B \ ^1\Sigma_u^+(4, 1)$ and $\text{GK} \ ^1\Sigma_g^+(0, 2)$ ($\tau \approx 58$ ns [56]) intermediate states, respectively. For Rydberg states converging to the $N^+ = 6$ threshold of H_2^+ , the $X \ ^1\Sigma_g^+(0, 2)$, $B \ ^1\Sigma_u^+(4, 3)$ and I^+

$\ ^1\Sigma_g^+(0, 4)$ ($\tau \approx 15$ -20 ns, determined using a pump-probe scheme analogous to that used in Ref. [56]) states are used. In this case, the $I^+(0, 4)$ state is chosen instead of the $\text{GK}(0, 4)$ state because of its much stronger transitions to $nf6$ Rydberg states. Accessing the $I^+(0, 4)$ state in a two-photon process requires using the rotationally excited $X \ ^1\Sigma_g^+(0, 2)$ state, which is weakly populated in a supersonic expansion, as a starting level. When the $\text{GK}(0, 0)$ state is used as intermediate state, the excitation to nf Rydberg states is restricted to states with $J = 1$. Transitions from the $\text{GK}(0, 2)$ and $I^+(0, 4)$ levels provide access to Rydberg states with total angular momentum quantum number $J = 1-3$ and $J = 3-5$, respectively. However, the only strong and narrow spectral lines correspond to $nf4(J = 1)$ and $nf6(J = 3)$ Rydberg states.

The experimental apparatus and measurement procedure are similar to those described in detail in Ref. [57]. They are therefore only briefly summarized here. A pulsed (repetition rate 25 Hz) skimmed supersonic expansion of pure H_2 is emitted from a valve held at 60 K for the experiments using the ground rovibrational $X(0, 0)$ state as a starting level. Because cooling to 60 K depletes the occupation probability of the $X(0, 2)$ level to below 0.1%, the valve is held at room temperature in the experiments accessing $nf6(J)$ Rydberg states. Nonetheless, the partial cooling of the rotational degrees of freedom in the supersonic expansion strongly reduces the density of $X(0, 2)$ rotationally excited molecules in the photoexcitation region. Consequently, the spectra of the $nf6$ Rydberg states have a much lower signal-to-noise ratios than those of $nf2$ and 4 Rydberg states.

The intermediate GK and I^+ states are accessed using pulsed vacuum-ultraviolet (VUV, $\lambda \approx 105$ nm) and

visible (VIS, $\lambda \approx 613$ nm or 580 nm) laser radiation, as detailed in Ref. [57]. The Rydberg states are excited from the selected GK or I^+ intermediate levels using a single-mode continuous-wave (cw) Ti:Sa laser (λ between 750 and 780 nm) with a bandwidth of 100 kHz. To achieve a high absolute frequency accuracy ($\Delta\nu/\nu$ in the order of $2 \cdot 10^{-11}$), the cw-laser frequency is stabilized to a frequency comb that is referenced to a Rb oscillator disciplined by a Global-Positioning-System receiver. To minimize systematic uncertainties arising from first-order Doppler shifts, the cw-laser beam intersects the molecular beam at near right angles and the laser beam is retroreflected by a mirror placed beyond the photoexcitation region. A small deviation angle α from 90° is intentionally maintained, resulting in each spectral line having two Doppler components with first-order Doppler shifts $\pm(v \sin \alpha/c) \nu_{\text{laser}}$ of equal magnitude but opposite sign. The first-order Doppler-free transition frequencies are obtained as averages of the fitted central positions of the two Doppler components. To ensure precise retroreflection and wavefront retracing, the laser beam is focused at the reflection mirror with a lens system of large effective focal length and the incoming and retroreflected laser beams are aligned at a distance of ≈ 12 m from the mirror, resulting in a retroreflection-angle control of better than $100 \mu\text{rad}$ [57].

To reduce systematic uncertainties from dc-Stark shifts, residual stray electric fields are compensated in three dimensions by applying well-controlled dc electric fields in the photoexcitation region and minimizing the Stark shifts, as explained in Refs. [57, 58]. Pulsed electric fields are used to extract the H_2^+ ions generated by autoionization of the Rydberg states located above the $X^+(0,0)$ ionization threshold towards a microchannel-plate (MCP) detector. These fields also field ionize long-lived Rydberg states, including those located below the $X^+(0,0)$ ionization threshold, and extract the resulting ions for detection. The spectra are recorded by monitoring the H_2^+ -ion current at the MCP detector as a function of the frequency of the cw laser.

III. QUALITATIVE ASPECTS OF THE ENERGY-LEVEL STRUCTURE AND EXPERIMENTAL RESULTS

The energy-level structure of nf Rydberg states belonging to series converging to excited rotational levels of the $X^+ \ ^2\Sigma_g^+$ ground electronic state of para- H_2^+ is depicted schematically in Fig. 2. Nuclear spins do not contribute to the structure of even- N^+ , low- v^+ levels of the $X^+ \ ^2\Sigma_g^+$ electronic ground state of H_2^+ because nuclear-spin symmetry is conserved in these states and even- N^+ states have $I = 0$ total nuclear spin. The level structure is determined by the relative strengths of the interactions that couple the rotational angular momentum \vec{N}^+ of the ion core, the core-electron spin \vec{S}^+ , and the orbital angular momentum $\vec{\ell}$ and the spin \vec{s} of the Rydberg

electron. These interactions are (i) the exchange interaction between the Rydberg and ion-core electrons, which causes a splitting between singlet $S = 0$ and triplet $S = 1$ states; (ii) the long-range charge-quadrupole and polarization electrostatic interactions that couple $\vec{\ell}$ and \vec{N}^+ ; (iii) the spin-orbit interactions that couple $\vec{\ell}$ with \vec{s} and \vec{S}^+ ; and (iv) the spin-rotation interaction and higher-order spin-orbit interactions that couple \vec{N}^+ and \vec{S}^+ in the ion core.

The strengths of interactions (i)-(iii) are proportional to the Rydberg-electron density in the H_2^+ -core region and thus scale with the principal quantum number n as n^{-3} . The spin-orbit interactions (iii) are several orders of magnitude weaker than interactions (i) and (ii). They are so weak in the nf Rydberg states with $n > 50$ of interest here that their effects on the level structure are not observable within the limits of our experimental resolution and sensitivity. They are therefore neglected in the following. The spin-rotation interaction (iv) and the ion-core rotational spacings are properties of the ion core and therefore n -independent. Consequently, interactions (i) and (ii) are expected to determine the main patterns of the level fine structure at low- n values, whereas interaction (iv) is expected to determine its main patterns at high n values.

Panels (a) and (c) of Fig. 2 display the angular-momentum coupling schemes corresponding to these two, low- n and high- n , limiting situations, as well as the resulting qualitative energy-level diagrams for $N^+ = 2$. For Rydberg states with n up to about 50 [panel (a)], the electrostatic coupling between $\vec{\ell}$ and \vec{N}^+ dominates, such that N ($\vec{N} = \vec{\ell} + \vec{N}^+$) is a good quantum number and the levels form groups that can be labeled by the value of N ($N = 1 - 5$ for $nf2$ series). Within each group, the exchange interaction further splits the structure according to the spin multiplicity, the singlet $J = N$, $S = 0$ level being located below the triplet $J = N$, $N \pm 1$, $S = 1$ levels. Singlet-triplet mixing among the two close-lying components of the same N values is already significant at this n value. At $n \approx 130$, the spin-rotation interaction in the ion core (interaction (iv)) becomes dominant and decouples $\vec{\ell}$ from \vec{N}^+ and \vec{s} from \vec{S}^+ . J^+ ($\vec{J}^+ = \vec{N}^+ + \vec{S}^+$) becomes the pattern-determining quantum number, giving rise to two groups of levels with $J^+ = 3/2$ and $5/2$ separated energetically by the spin-rotation splitting of the $N^+ = 2$ ion-core level [panel (c)]. Within these groups, the levels are further split by the electrostatic interaction (ii) which couples J^+ with $\vec{\ell}$ to form \vec{J}_s . The Rydberg-electron spin is almost fully decoupled in this situation and the levels occur as pairs of near-degenerate states with $J = J_s \pm 1/2$.

In the treatment of the level structure of H_2 Rydberg states by MQDT, interactions (i)-(iv) and the evolution of the level structure from the low- n to the high- n case are accounted for by the values of the quantum-defect parameters and the ion-core level structure used in the calculations and which can be determined from fits to

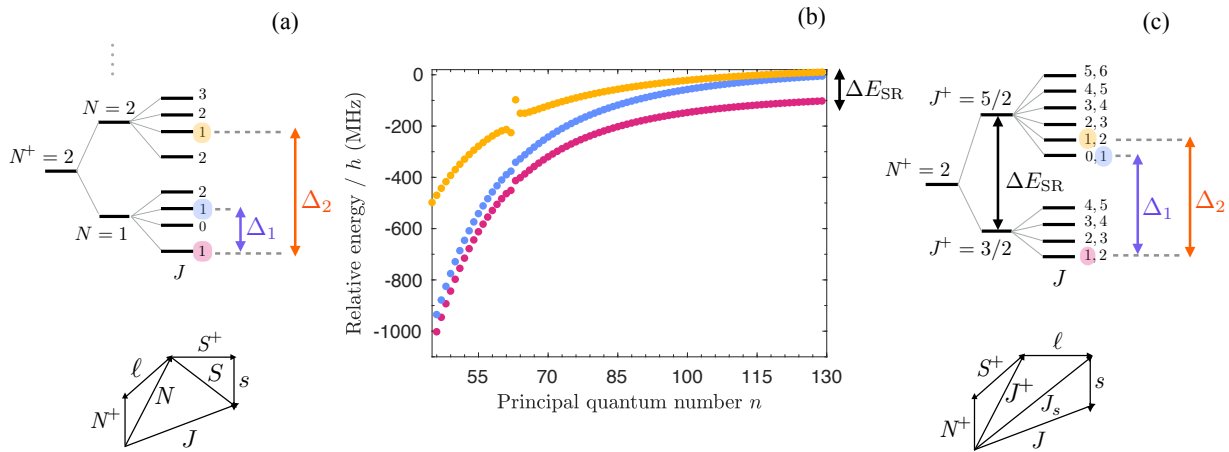


Figure 2. (a) and (c) Qualitative energy-level diagrams and angular-momentum coupling schemes corresponding to f Rydberg states of H_2 with an $N^+ = 2$ ion core, for low n ($n < 50$) and high n ($n > 130$), respectively. Δ_1 (purple) and Δ_2 (orange) designate the spacings between the three $J = 1$ fine-structure components. (b) Evolution, from low to high n values, of the positions of the three $nf2(J = 1)$ Rydberg states relative to the zero-quantum-defect positions $-cR_{\text{H}_2}/n^2$, obtained in an MQDT calculation including electron spins. The magenta, blue, and yellow dots designate these three states in order of increasing energy, as displayed in panels (a) and (c). The double-headed arrow indicates the spin-rotation splitting of the $N^+ = 2$ ion core, shown on an expanded scale in panel (c).

experimentally observed level positions or in ab initio calculations [24, 39], as explained further in Section IV. As illustration of this evolution, Fig. 2(b) shows the level structure of $nf2(J = 1)$ Rydberg states obtained in an MQDT calculation including electron spins based on quantum-defect parameters extracted from the recent high-level ab initio calculations of low- n Rydberg states [44–47], as explained in Section IV A. The calculated energies of the three $J = 1$ fine-structure components are shown as magenta, blue, and yellow dots, in order of increasing energies at each value of n . The intervals between these three components change with the principal quantum number n because the hierarchy of angular-momentum coupling gradually changes between the situations depicted schematically in panels (a) and (c). At $n = 50$, the largest energy separation is between the two almost degenerate states with $N = 1$ (magenta and blue dots) and the state with $N = 2$ (yellow dots). As n increases, the two $N = 1$ states split, and the energy of the middle component (blue dots) starts approaching that of the highest-energy state (yellow dots). At $n \approx 130$, the pattern consists of one single level at low energies, which can be associated with the lower ($J^+ = 3/2$) ion-core spin-rotational component, and a doublet at high energies corresponding to the upper ($J^+ = 5/2$) ion-core spin-rotational component. This change in behavior is the result of the n -independent spin-rotation interaction (iv) becoming dominant over interactions (i) and (ii), which both scale as n^{-3} , as explained above. As $n \rightarrow \infty$, the splitting between the states with $J^+ = \frac{3}{2}$ and with $J^+ = \frac{5}{2}$ converges to the spin-rotation splitting of the $N^+ = 2$ H_2^+ ion-core level, which is indicated in panel (b) by the double-headed arrow. The local pertur-

bation in the energy-level structure centered around the $6f2(J = 1)$ states in panel (b) is the effect of a rotational-channel interaction with the $16f4(J = 1)$ states.

The behavior of the three components for each of the $nf4(J = 1)$ and $nf6(J = 3)$ states is similar to that just discussed for the $nf2(J = 1)$ states and is illustrated in Figs. S1 and S2 of the supplemental material, respectively. The main difference is that the spin-rotation splitting of the ion core increases with N^+ [see Eq. (1)], so that the limiting situation illustrated by Fig. 2(c) is reached at lower n values. The energy-level structures of nf Rydberg states with different values of J show similar patterns and can be rationalized using the same angular-momentum-coupling arguments. Transitions to these Rydberg states are, however, weak and significantly broadened by autoionization, and therefore not analyzed further.

As typical examples of the spectral patterns just discussed, Fig. 3 depicts spectra of $nf2(J = 1)$ Rydberg states at $n = 54$ (a) and $n = 80$ (b) recorded from the GK(0,0) intermediate level, and $nf4(J = 1)$ Rydberg states at $n = 46$ (c) and $n = 52$ (d) states recorded from the GK(0,2) level. These spectra consist of three pairs of lines, each corresponding to the two Doppler components of a transition to a specific fine-structure level. The colored vertical lines, with color code corresponding to Fig. 2, indicate the first-order-Doppler-free positions. These positions are determined from fitting Voigt line profiles to the spectral lines. Their full widths at half maximum are all in the range between 6 and 9 MHz and are only slightly larger than the widths of 5 MHz obtained in measurements of nf series converging to the $N^+ = 0$ level of H_2^+ [57]. This line broadening is attributed to rotational autoionization because all final states of these transitions

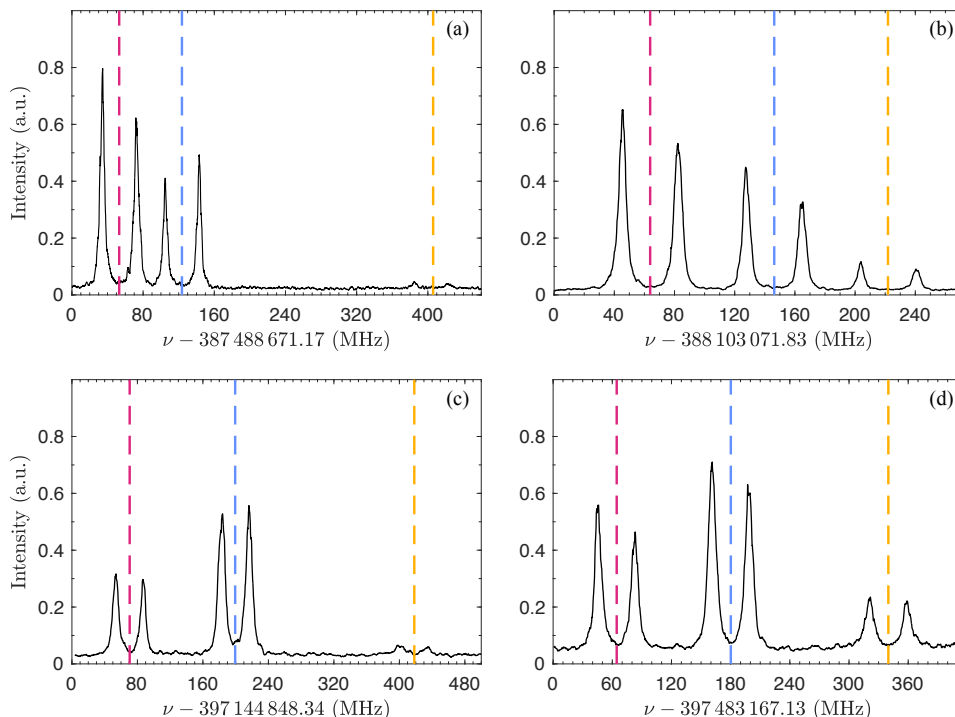


Figure 3. Spectra of the $54f2(J=1) \leftarrow \text{GK}(0,0)$ (a), $80f2(J=1) \leftarrow \text{GK}(0,0)$ (b), $46f4(J=1) \leftarrow \text{GK}(0,2)$ (c), and $52f4(J=1) \leftarrow \text{GK}(0,2)$ (d) transitions. The vertical dashed lines indicate the fitted Doppler-free transition frequencies for each of the three fine structure components with $N^+ = 2$, $J = 1$ ($N^+ = 4$, $J = 1$). The color coding of the vertical lines corresponds to that shown in Fig. 2.

have rotationally excited H_2^+ ion cores and lie above the lowest ionization threshold of H_2 , corresponding to the $X^+(v^+ = 0, N^+ = 0)$ ground state of H_2^+ .

In Fig. 3(a), corresponding to the low- n coupling situation, the transitions to the lowest two fine-structure components of the $54f2(J=1)$ Rydberg state are strong and the transition to the third component is much weaker. The lowest two components are the two $N = 1$ states of mixed singlet-triplet character [see Fig. 2(a)] that can be reached in a single-photon transition from the GK $^1\Sigma_g^+$ state with $N = 0$. In the approximation of N being a good quantum number, the third component with $J = 1$ is a triplet state with $N = 2$, which is not optically accessible from the $N = 0$ starting level. Weak lines are nevertheless observed for this transition, because at $n = 54$ the spin-rotation interaction in the ion-core already slightly mixes states of different N values. At $n = 80$ [panel (b)], corresponding to an intermediate situation between the low- and high- n coupling situations, the transitions to all three fine-structure components exhibit comparable intensities, because the spin-rotation interaction in the ion core already significantly mixes singlet and triplet states of different N values (see Fig. 2(c)). The spectrum of the $110f2(1)$ states displayed in Fig. 4 was recorded without the back-reflected beam and consists of one Doppler component per transition. It corresponds to the high- n coupling situation. The spectral pattern exhibits a main splitting, given by the ion-core spin-rotation interval, be-

tween the lower component and the upper two close-lying components, as expected from Fig. 2(b).

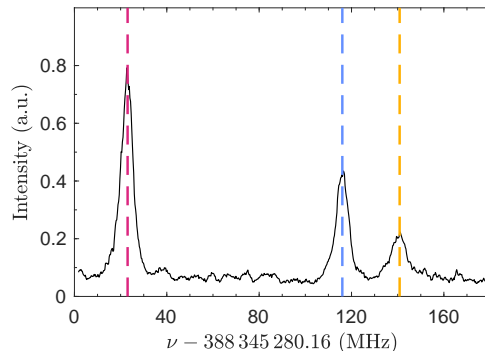


Figure 4. Spectrum of the $110f2(J=1) \leftarrow \text{GK}(0,0)$ transition measured without the retroreflected beam. The vertical dashed lines indicate the fitted transition frequencies for each of the three fine structure components with $N^+ = 2$, $J = 1$, corresponding to the measured Doppler component. The color coding of the vertical lines corresponds to that shown in Fig. 2.

The spectra of the $46f4(J=1)$ and $52f4(J=1)$ states displayed in Figs. 3(c) and (d), respectively, display a similar behavior as the $nf2(J=1)$ states, with the difference that the "forbidden" transition to the highest ($N = 2$) fine-structure component is already significant

at n values below 54. This difference originates from the larger spin-rotational splitting of the $N^+ = 4$ ion core level, as already discussed above.

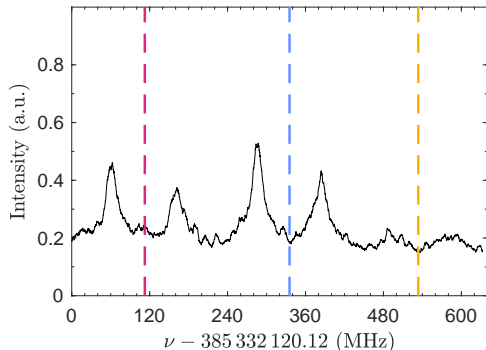


Figure 5. Spectrum of the $46f6(J=3) \leftarrow I^+(0,4)$ transition. The vertical dashed lines indicate the fitted Doppler-free transition frequencies for each of the three fine structure components with $N^+ = 6$, $J = 3$. The color coding of the vertical lines corresponds to that shown in Fig. 2.

The spectrum of the $46f6(J=3) \leftarrow I^+(0,4)$ transition, displayed in Fig. 5, also consists of three pairs of lines with Doppler-free transition frequencies indicated by colored dashed vertical lines using the same color coding as in Figs. 2 and 3. Compared to the spectra of Rydberg states with $nf2$ and $nf4$ Rydberg states discussed above, the full widths at half maximum of about 25 MHz are significantly larger and the signal-to-noise ratio is strongly reduced. The increase in linewidths is attributed to the shorter lifetime ($\tau \approx 15\text{-}20$ ns) of the $I^+(0,4)$ state, corresponding to a Lorentzian contribution of $\approx 8\text{-}11$ MHz, and to the lower quality and broader transverse-velocity distribution of the supersonic expansion caused by the valve being held at room temperature instead of 60 K to enhance the population of the $J = 2$ ground state rotational level, as explained in Section II. Moreover, the lifetime of the $I^+(0,4)$ state is comparable to the pulse length of the VIS laser (≈ 8 ns) used to access the Rydberg states starting from the I^+ state. Therefore, the excitation to Rydberg states takes place to a significant extent while the pulsed VUV and VIS lasers are on, which can result in ac-Stark broadening and shifts (see below).

The frequencies of numerous transitions to $nf2(J=1)$, $nf4(J=1)$, and $nf6(J=3)$ Rydberg states converging to $X^+ 2\Sigma_g^+(v^+ = 0, N^+ = 2, 4, 6)$ rotational levels of H_2^+ were measured in the range of principal quantum number n between 28 and 115 and the results are summarized in panels (a)-(c) of Fig. 7 below. These frequencies are the input required to determine the rotational and spin-rotational fine structure of the H_2^+ ion core in the MQDT fits and the quantification of their uncertainties is of key importance in the present work. Each frequency was obtained as the average of several measurements carried out after full realignment of the optical setup. In this way, the systematic uncertainties caused by residual first-

order Doppler shifts average out and can thus be treated as statistical.

Table I. Error budget and frequency corrections with the example of the determination of the transition frequency to the lowest-energy fine-structure component of the $54f2(J=1)$ state from the GK(0,0) intermediate level (measured frequency $\tilde{\nu}_{\text{laser}} = 12925.232\,572\text{ cm}^{-1}$) from a set of independent measurements after complete realignment of the optical setup. All values and uncertainties are reported in kHz.

	$\Delta\nu$	σ_{stat}	σ_{sys}
Lineshape fits and residual 1 st -order Doppler shift		250	
2 nd -order Doppler shift	+2		0.5
dc Stark shift			25
ac Stark shift			<5
Zeeman shift			<10
Pressure shift			<1
Photon-recoil shift	-165		

The error budget for a typical transition frequency is presented in Table I. The main contribution to the overall uncertainty (250 kHz) is statistical and originates, in almost equal parts, from the intrinsic uncertainties in the determination of the line centers through fits of the line shapes with Voigt profiles and from the distribution of the residual first-order Doppler shifts. The systematic uncertainties corresponding to the $54f2(J=1) \leftarrow \text{GK}(0,0)$ transition are also listed in Table I. They were determined in series of measurements in which the experimental conditions (laser intensities, beam velocity, valve stagnation pressure) were systematically modified. In the case of transitions to $nf2(J=1)$ and $nf4(J=1)$ states, the systematic uncertainties are much smaller than the statistical ones and do not exceed 25 kHz. As discussed above, the measurements of the transition frequencies to the $nf6(J=3)$ states are possibly affected by ac-Stark shifts caused by the pulsed laser radiation during the short lifetime of the I^+ state. It was not possible to fully quantify these shifts in our experiments, but we estimate the maximum possible systematic uncertainty to be 5 MHz and we include this contribution when determining the systematic uncertainty of the $X^+(0,6) - I^+(0,4)$ interval (see Table II in Section IV B). All transition frequencies determined in this work, after correcting for their precisely known second-order Doppler shifts (+2 kHz) and the photon-recoil shifts (-165 kHz), are listed in the supplemental material.

The energy intervals between the GK(0,0), GK(0,2) and $I^+(0,4)$ states needed to derive a common relative energy scale for the $nfN^+(J)$ Rydberg states are listed in Table II. The relative position of the GK(0,0) and GK(0,2) is known with sufficient accuracy from earlier work [57]. The relative position of the $I^+(0,4)$ and GK(0,2) states was determined by measuring the transition frequencies from each of these two states to the $56f4(J=3)$ Rydberg state. This state lies in close proximity of, and interacts with, the $13f6(J=3)$ Rydberg

state, and the resulting mixed $N^+ = 4$ and 6 character makes this state accessible in one-photon transitions from both the $I^+(0, 4)$ and the $GK(0, 2)$ levels. The low population of the $X(0, 2)$ level of H_2 used to access the $I^+(0, 4)$ state, however, limited the signal-to-noise ratio of the spectrum of the $56f4(J = 3) \leftarrow I^+(0, 4)$ transition. Consequently, the interval between the $I^+(0, 4)$ and $GK(0, 2)$ levels could only be determined with an uncertainty of 2 MHz.

IV. MQDT ANALYSIS

Over the years, MQDT, which was initially introduced to explain autoionization and perturbations caused by rotational channel interactions in the Rydberg spectrum of H_2 [20, 21], has been continuously refined and extended to account for the structure and dynamics of molecular Rydberg states and to determine accurate molecular ionization energies [22, 24, 26–40]. In the case of molecular hydrogen, a consistent set of quantum-defect parameters, derived from ab initio calculations of low-lying Rydberg states and fits to experimentally observed line positions, has been established that can describe the np and nf series with high accuracy, including subtle effects related to the fine and hyperfine structures [36, 59, 60].

The recent possibility to calculate the potential energy functions of the low-lying Rydberg states of H_2 up to $n \approx 10$ ab initio with almost arbitrary accuracy [44–46] opens a route to the determination of full sets of quantum-defect parameters, including their energy dependence, following procedures established by Jungen and his coworkers [36, 39, 61–64]. To analyze the data on nf Rydberg states presented in the previous section, we use a new set of quantum-defect parameters determined from recent high-level calculations of the low-lying Rydberg states of H_2 [44–47]. Given the exceptional accuracy of these calculations, with estimated uncertainties in the order of 10 MHz at $n = 8$, and the n^{-3} scaling of the errors in the positions calculated from quantum defects, these quantum-defect parameters are expected to be sufficiently accurate to describe the positions of high-lying Rydberg states (with 40 kHz accuracy at $n=50$), except in the vicinity of perturbations involving low-lying Rydberg states with vibrationally excited ion cores, as detailed in Section IV B.

In the following, we briefly summarize the MQDT formalism used to calculate the positions of high-lying nf Rydberg states for comparison with the experimental results and we present the main features of the new quantum-defect parameters. All calculations were performed using the MQDT-programs developed over several decades in the group of Christian Jungen.

A. MQDT Formalism and Quantum Defects Parameters

The term value T_n of a Rydberg state with principal quantum number n is given by

$$T_n = \frac{E^+(v^+, N^+, J^+)}{hc} - \frac{\mathcal{R}_{H_2}}{(n - \bar{\mu})^2}, \quad (4)$$

where E^+ is the ionization energy and $\bar{\mu}$ the effective quantum-defect of this specific Rydberg channel.

For $n\ell$ Rydberg states, the MQDT formalism allows the determination of the effective quantum-defect in Eq. (4) for all possible combinations of vibrational and rotational excitation in the ion core and for all possible combinations of the spin of the core and the Rydberg electron using the concept of a *frame transformation* [20, 27, 35]. This concept is based on the idea, that the scattering Rydberg electron and the ion core can be described in Hund's case (b), while the Rydberg equation in (4) assumes Hund's case (d) coupling.

In the specific case of a Rydberg electron with $\ell = 3$ and $s = 1/2$ and the ion core in the $^2\Sigma_g^+$ state, $\Lambda = 0, 1, 2$ and 3 for $S = 0, 1$ ($\vec{S} = \vec{S}^+ + \vec{s}$). This results in 8 eigenquantum defects $\mu_f^{(S\Lambda)}$ for the description of f Rydberg states in para- H_2 (note: (i) we neglect the nuclear spin because $I = 0$ in para- H_2) and (ii) the quantum defects have no dependence on Ω [36]).

The quantum defects depend on the internuclear distance R and the energy of the Rydberg electron ε . Following the treatment of the p Rydberg states in Ref. [38], they can be represented as 24 functions of the internuclear distance:

$$\mu_f^{(S\Lambda)}(R, \varepsilon = 0), \frac{d\mu_f^{(S\Lambda)}(R, \varepsilon = 0)}{d\varepsilon}, \frac{d^2\mu_f^{(S\Lambda)}(R, \varepsilon = 0)}{d\varepsilon^2}. \quad (5)$$

The eigenquantum defects and their energy derivatives are evaluated at the ionization threshold, i.e., for zero binding energy of the Rydberg electron.

In Ref. [36], eigenquantum-defect functions for f Rydberg states were extracted from a polarization model, which does not distinguish between singlet and triplet ion-core-Rydberg-electron scattering. In addition, the polarization model assumes a multipole expansion for the ion core and diverges for larger R values. However, the model enables the calculation over a large range of principal quantum numbers, which results in a better extrapolation of the quantum defects to $\varepsilon = 0$.

While the R -dependence of the eigenquantum defects predominantly affects the positions of vibrational interlopers, the Λ - and S -dependence has an impact on the spin-rotational structure of the Rydberg states, which represents one of the main topics of this work.

The extraction of the quantum defects from the available ab initio data follows the procedure described in Ref. [38] and a more detailed account will be given in a future publication [47]. In short, the PES are converted

to $\mu_\ell^{(SA)}(R, n)$, which enables the identification of the states with f character and distinguishes them from the p (larger quantum defect) and h (smaller quantum defect) states. For each value of the internuclear distance R , the quantum defects for a given (SA) pair are extrapolated to $n = \infty$ using a second-order polynomial, corresponding to the zero-energy quantum defect $\mu_f^{(SA)}(R, \varepsilon = 0)$. For $\varepsilon = 0$, the μ -quantum defects correspond to the η -quantum defects, introduced by Ham [65] to avoid unphysical solutions when applying the MQDT quantization condition. The energy dependence of the η -defects is encoded similarly to the one in Eq. (5) and is obtained in a least-squares adjustment using the μ -defects at $\varepsilon = 0, -1/(2\nu_i^2)$, where ν_i are the effective quantum numbers for the ab initio curves with $n = 4, 5, 6, 7, 8$.

While the η defects avoid the issues related to unphysical interlopers, they show a stronger energy-dependence than the μ defects in the case of H_2 . To mitigate this effect, the MQDT program uses functions of the form $A_f(\varepsilon)\eta_f^{(SA)}(R, \varepsilon)$, where $A_f(\varepsilon)$ is the Ham scaling factor, when constructing the MQDT matrices for a given energy.

B. MQDT Fits of Spin-Rotation and Rotational Intervals

MQDT calculations based on the ab initio quantum-defect parameters introduced in Subsection IV A were used to determine the rotational and spin-rotational level structure in the $X^+(v^+ = 0)$ ground state of H_2^+ in a least-squares fit to the positions of the $nf2(J = 1)$, $nf4(J = 1)$ and $nf6(J = 3)$ Rydberg states determined as explained in Section III. As an example, Fig. 6 displays the results of an MQDT calculation (light blue line) in comparison to the measured positions (blue dots) of the middle fine-structure component (color coding corresponding to that shown in Fig. 2) of the $nf2(J = 1)$ states (see below for a discussion of the energy perturbations around $n = 40$ and $n = 62$). An iterative fitting procedure was adopted, with separate fits of the spin-rotational intervals of H_2^+ for fixed values of the pure (spin-free) rotational intervals, and of the spin-free rotational intervals for fixed values of the spin-rotational intervals. The advantages of this procedure for the determination of the H_2^+ spin-rotational intervals are that (i) the fine-structure splittings of the nfN^+ Rydberg states of H_2 are not sensitive to the exact positions of the H_2^+ rotational levels, as long as the series are free of perturbations from rotational channel interactions, (ii) the spin-rotational splitting in H_2^+ can be reliably derived from the fine-structure splittings of the nf Rydberg states without the need to know their absolute energies accurately, (iii) the transition frequencies needed to access different fine-structure components of a given nfN^+ state from a given intermediate state are almost identical and subject to the same first-order Doppler shifts, and finally (iv) the fine-structure components of a given nfN^+ state

have similar polarizabilities and thus similar Stark shifts. As a result of (iii) and (iv), the residual Stark and first-order Doppler shifts and their associated uncertainties cancel out when determining the fine-structure splittings as differences between transitions frequencies to different fine-structure components of any given nfN^+ state. Reliable fine-structure intervals can therefore be determined at n values beyond 100 and used to determine the H_2^+ spin-rotational intervals. The determination of the pure rotational energies of H_2^+ in an MQDT least-squares fit requires precise values of the absolute transition frequencies and does not benefit from these advantages, but is more efficient once the spin-rotational intervals of the H_2^+ rotational levels have been determined.

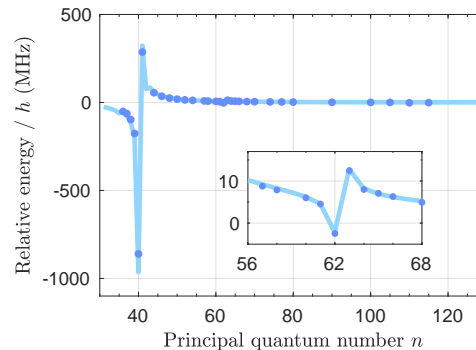


Figure 6. MQDT-calculated (light blue line) and experimentally obtained (colored dots) binding energies of the middle fine-structure component (color coding corresponding to that shown in Fig. 2) of the $nf2(J = 1)$ Rydberg states. All binding energies are referenced to the energies of the corresponding unperturbed nf series.

The results of the least-squares fits are the extrapolated positions of the spin-rotational and rotational levels of H_2^+ with respect to the positions of the $GK(0,0)$, $GK(0,2)$ and $I^+(0,4)$ intermediate states used to record the spectra of the $nf2(J = 1)$, $nf4(J = 1)$ and $nf6(J = 3)$ Rydberg series. The energies of all fine-structure components of the measured nfN^+ Rydberg series with respect to their corresponding ionization limits are computed in an MQDT calculation including the effects of electron spins as explained in Ref. [51], see also [35, 66]. Adding these Rydberg-electron energies to each of the corresponding observed transition frequencies from the selected intermediate states yields independent values for the binding energy of that intermediate state. The residuals shown in Fig. 7 are computed as the differences between these independent values and their weighted averages, which represent the $X^+(0,2) - GK(0,0)$, $X^+(0,4) - GK(0,2)$ and $X^+(0,6) - I^+(0,4)$ energy intervals. The weights of individual contributions are the inverse squares of the experimental uncertainties [see vertical error bars in Fig. 7(d)-(f)].

Figs. 7(a)-(c) present an overview of the residuals obtained from all measured transitions to $nf2(J = 1)$, $nf4(J = 1)$ and $nf6(J = 3)$ Rydberg states, respectively.

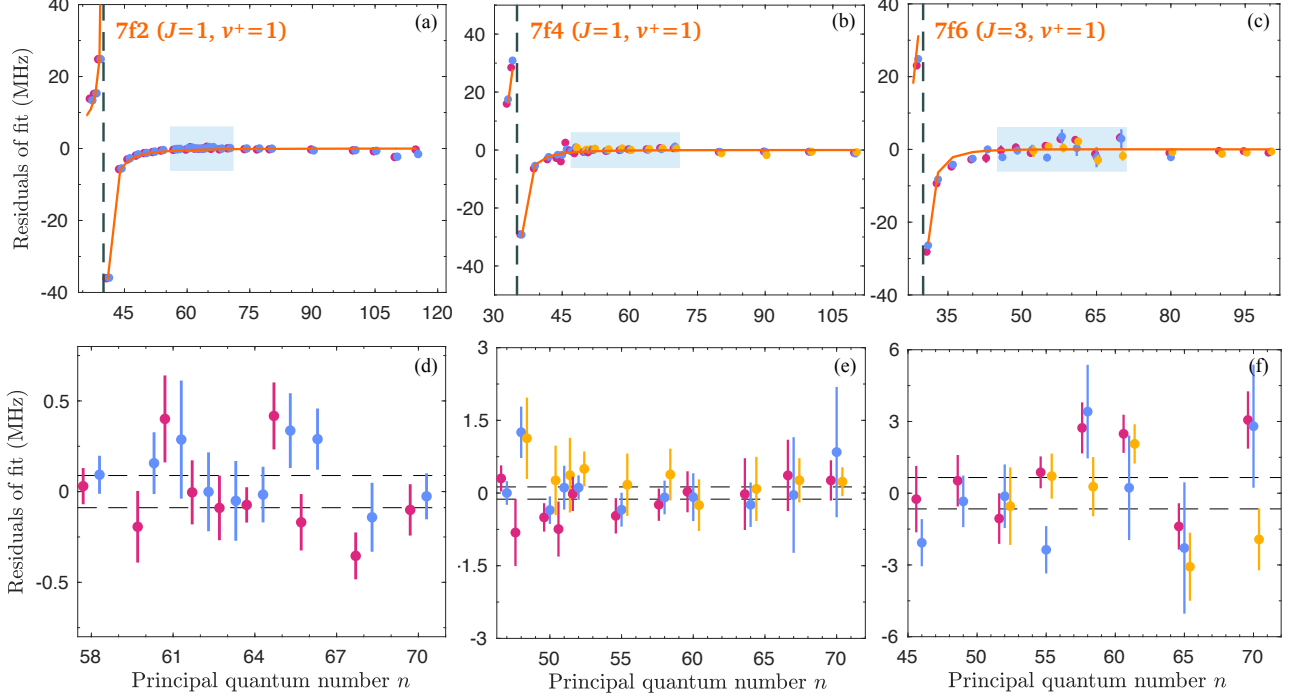


Figure 7. Residuals of the binding energies $X^+(0,2) \leftarrow \text{GK}(0,0)$ [(a),(d)], $X^+(0,4) \leftarrow \text{GK}(0,2)$ [(b),(e)], and $X^+(0,6) \leftarrow I^+(0,4)$ [(c),(f)]. The color coding of the data points representing different fine-structure components corresponds to that shown in Fig. 2. Panels (a)-(c) show the entire range of nf states which were experimentally probed. The vertical grey lines indicate the positions of the $7f2(J=1)$, $7f4(J=1)$, and $7f6(J=3)$ ($v^+=1$) Rydberg states, which cause perturbations in the residuals. The orange lines indicate the residuals obtained in a simple two-channel model of the interaction between the $nfN^+(v^+=0)$ series and the $7fN^+(v^+=1)$ perturbers (see text for details). The blue rectangles in panels (a)-(c) show the selected ranges of principal quantum numbers which were used to extract the reported values of the $X^+(0,2) \leftarrow \text{GK}(0,0)$, $X^+(0,4) \leftarrow \text{GK}(0,2)$ and $X^+(0,6) \leftarrow I^+(0,4)$ binding energies. The residuals obtained after correction with the two-channel model are shown on an expanded scale in panels (d)-(f), in which the horizontal dashed lines indicate the standard deviations of the datasets in each case.

Most residuals are within the experimental uncertainties and significantly below 1 MHz, confirming the accuracy of the MQDT parameters expected from the considerations presented in Subsection IV A. However, residuals up to ± 40 MHz between measured and calculated positions are observed for each series near the calculated positions of the $7f(v^+=1)$ Rydberg states of the corresponding N^+ and J values, i.e., $7f2(J=1, v^+=1)$, $7f4(J=1, v^+=1)$ and $7f6(J=3, v^+=1)$, as indicated by the dashed grey vertical lines. These low- n states with vibrationally excited ion-cores cause strong perturbations of the Rydberg series through interactions between channels of the same N^+ , ℓ and J values but differing in v^+ by ± 1 .

As explained in Subsection IV A, these channel interactions should be accurately described by the quantum-defect parameters derived from ab initio calculations. Indeed, Fig. 6 shows that the MQDT calculations reproduce the ≈ 1 GHz experimental shifts caused by the $7f2(J=1, v^+=1)$ perturber in the region around the $40f2(J=1, v^+=0)$ state to a level of 95% accuracy. The reason for the inability of the MQDT calculations to

exactly reproduce the level structure close to the low- n perturbing states does not lie in the inaccuracy of the quantum-defect parameters. Instead, it originates from a problem in the definition of the energy of the Rydberg electron arising from the energy dependence of the quantum defects when levels with ion cores in different rovibrational states interact [24, 48]. In situations involving a single channel, or two channels associated with energetically close-lying ion-core states, the Rydberg electron has a well defined binding energy and the values of the quantum defects can be accurately determined using the energy-dependent quantum-defect parameters determined ab initio. As illustration, the inset of Fig. 6 displays the ≈ 10 MHz energy shifts in the region around the $62f2(J=1)$ state, which are caused by a rotational-channel interaction with the $16f4(J=1)$ state. The MQDT calculations perfectly reproduce these shifts, as confirmed by Fig. 7 (a), in which the residuals show no effect of the rotational perturber. In contrast, if two channels with very different ion-core energies interact [as is the case for the perturbations caused by the $7f(v^+=1)$ states], the Rydberg-electron binding energy,

and thus the value of the energy-dependent quantum defect parameters, depend on the ion-core level used as origin of the energy scale [24, 48–50]. In standard MQDT calculations, this problem of the energy scale is avoided by referencing the electron binding energy to the same energy (the mean of the two ion-core energies) when determining the values of the quantum defect parameters. This procedure, which makes the MQDT formalism efficient, is an approximation. It is physically motivated, in electron-(positive) ion systems, by the strongly attractive Coulomb potential which results in the electron having similar kinetic energies in the core region for channels associated with different ion-core states [24]. The effects of this approximation are usually not detected, either because the quantum-defect parameters and their energy dependence are not known with sufficient precision in the first place, or because the Rydberg spectra are not sufficiently resolved. In the present study, both the quantum-defect parameters and the experimental data in the energy regions close to the $v^+ = 1$ perturbers are of high accuracy, thus providing an ideal opportunity for a detailed characterization of the effects of the energy-reference ambiguity. The data shown in Fig.6 could therefore be used to test the performance of alternative vibrational frame transformations as introduced in Ref. [48–50].

Inspection of the functional form of the energy dependence of the residuals in Fig. 7(a)-(c) leads to the conclusions that (1) the effect of the vibrational-channel interaction is the same for all fine-structure components of a given state of principal quantum number n , so that the spin fine structure can be neglected in the following discussion; and (2) they closely reproduce the functional form of the level shifts caused by the perturbation (see Fig. 6). Consequently, the residuals can be accurately modeled using a simple two-channel interaction model, one consisting of an isolated resonance at the position of the low- n perturber, and the other of a Rydberg series with positions corresponding to the unperturbed positions of the high- n levels of the f series. Such a model involves three adjustable parameters: two quantum defects, one (η_{11}) to describe the position of the perturbing $7fN^+(v^+ = 1)$ level and the other (η_{00}) to describe the positions of the $nfN^+(v^+ = 0)$ series, as well as one channel-interaction parameter, an off-diagonal quantum defect η_{10} , which determines the overall amplitude of the residuals. The orange lines in Fig. 7(a)-(c) depict the residuals calculated with this two-channel model after optimization of the three parameters to the values of $\eta_{00} = 1.0 \times 10^{-5}$, $\eta_{11} = 2.3 \times 10^{-2}$, and $\eta_{10} = 1.41 \times 10^{-3}$. They perfectly describe the residuals of the MQDT calculations (colored dots). Moreover, the three sets of residuals can be modelled with the same set of three parameters, as expected for channel interactions that are all $\Delta v^+ = 1$, $\Delta N^+ = 0$, $\Delta \ell = 0$ interactions involving a $7f(v^+ = 1)$ perturbing level and high $nf(v^+ = 0)$ Rydberg states. Fig. 7 thus demonstrates that the energy-reference inconsistency of standard MQDT calculations can be corrected empirically using a two-channel interac-

tion model.

Figs. 7(d)-(f) present the residuals after this correction on an expanded scale in the range of principal quantum numbers used to determine the rotational and spin-rotational level structure of H_2^+ . States with principal quantum number beyond 70 were excluded from this analysis to limit the systematic uncertainties from dc Stark shifts caused by residual stray electric fields to less than 150 kHz, i.e., well within the statistical uncertainty of the measurements. The residuals do not show any trends over the displayed ranges of principal quantum numbers n and their distribution does not strongly deviate from a normal distribution. We therefore conclude that the combination of MQDT calculations based on the new set of ab initio quantum-defect parameters with an empirical two-channel interaction model to correct for the energy-reference inconsistency of standard MQDT near perturbations involving low- n Rydberg states can be used to determine ionization energies by extrapolation at a precision limited by the experimental uncertainties in the transition frequencies.

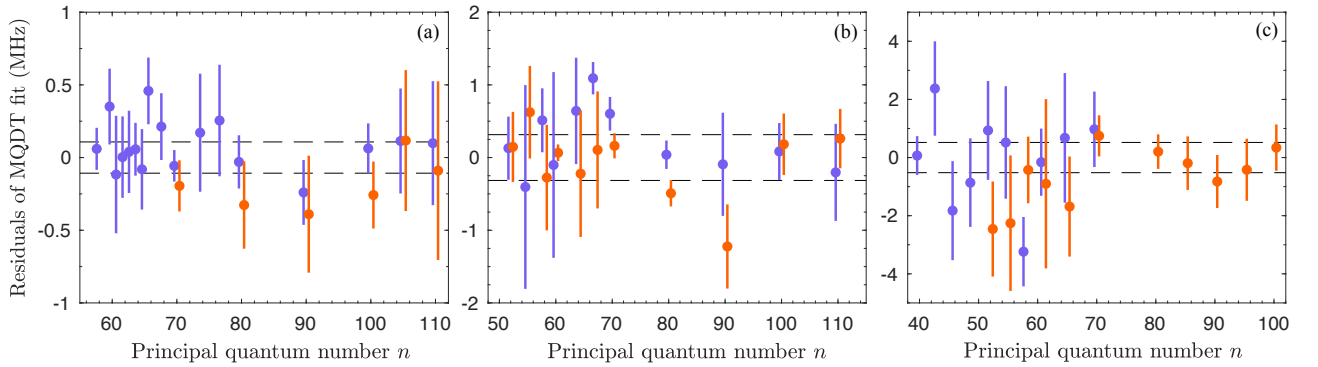
The upper part of Table II summarizes all energy intervals relevant to the determination of the spin-free term values of the rotational levels of the ground vibronic state of para- H_2^+ and their uncertainties. The lower part lists the experimental values of the three lowest rotational intervals of para- H_2^+ , which are determined here for the first time with such precision. More precise ab initio results by Korobov [3, 4] are also available for the two lowest rotational intervals. The experimental values obtained in this work are in excellent agreement, at the level of 1σ , with these ab initio results.

Many more transitions, to states with n values up to 115 (see, e.g., Fig. 4), could be used to determine the H_2^+ spin-rotation intervals $\Delta E_{SR}(N^+ = 2)$, $\Delta E_{SR}(N^+ = 4)$ and $\Delta E_{SR}(N^+ = 6)$, as explained above. In the fits, the least-squares deviations between the experimentally determined splittings Δ_1 and Δ_2 (see Fig. 2) between fine-structure components and the corresponding energy splittings calculated by MQDT for varying values of the spin-rotation coupling constant were minimized. Fig. 8 displays the fit residuals corresponding to Δ_1 in purple and to Δ_2 in orange, with the dashed lines indicating the standard deviations of the data sets. The increased error bars and the larger scatter of the experimental data obtained for the spin-rotation splitting of the $N^+ = 6$ level are the result of the poor signal-to-noise ratio of these spectra.

The spin-rotation coupling constants $\gamma_{SR}^{N^+=2}$, $\gamma_{SR}^{N^+=4}$ and $\gamma_{SR}^{N^+=6}$ are calculated from the optimized spin-rotation intervals using Eq. (1). $\gamma_{SR}^{(0)}$ and $\gamma_{SR}^{(1)}$ are determined in a least-squares fit from $\gamma_{SR}^{N^+=2}$, $\gamma_{SR}^{N^+=4}$ and $\gamma_{SR}^{N^+=6}$ using Eq. 2. The residuals of this fit are below 100 kHz, i.e. on the order of the uncertainties of $\gamma_{SR}^{N^+=2}$, $\gamma_{SR}^{N^+=4}$ and $\gamma_{SR}^{N^+=6}$, confirming the validity of Eq. (2). Table III lists all obtained values, which are determined here for the first time with a precision below 100 kHz for

Table II. Summary of energy intervals used to determine the first three rotational intervals in para-H₂⁺ and their uncertainties.

	Energy interval	Value (cm ⁻¹)	Ref.
(1)	X ⁺ (0, 0) – GK(0,2)	12 723.757 440 7(18) _{stat} (40) _{sys}	[43]
(2)	X ⁺ (0, 2) – GK(0,0)	12 962.876 609 0(30) _{stat}	This work
(3)	X ⁺ (0, 4) – GK(0,2)	13 299.213 073 2(42) _{stat}	This work
(4)	X ⁺ (0, 6) – I ⁺ (0,4)	12 905.184 142(22) _{stat} (170) _{sys}	This work
(5)	GK(0,2) – GK(0,0)	64.882 423 7(11) _{stat}	[56]
(6)	I ⁺ (0,4) – GK(0,2)	1009.958 87(7) _{stat}	This work
(7) = (5)+(6)	I ⁺ (0,4) – GK(0,0)	1074.841 29(7) _{stat}	This work
(8) = (2)–(1)–(5)	X ⁺ (0,2) – X ⁺ (0,0)	174.236 744 6(77)	This work
(9)	X ⁺ (0,2) – X ⁺ (0,0)	174.236 742 482 36	Theory [3, 4]
(10)	X ⁺ (0,2) – X ⁺ (0,0)	174.236 71(7)	[51]
(11) = (3)–(1)	X ⁺ (0,4) – X ⁺ (0,0)	575.455 632 5(86)	This work
(12)	X ⁺ (0,4) – X ⁺ (0,0)	575.455 640 795 85	Theory [3, 4]
(13) = (4)–(1)+(6)	X ⁺ (0,6) – X ⁺ (0,0)	1191.385 571(240)	This work

Figure 8. Residuals of the fitted energy intervals Δ_1 (purple dots) and Δ_2 (orange dots) (see also Fig. 2), displayed as the difference between the experimentally determined and MQDT-predicted energy intervals, for nf Rydberg states converging to the $N^+ = 2$ (a), $N^+ = 4$ (b), and $N^+ = 6$ (c) ionization thresholds. The horizontal dashed lines indicate the standard deviations of the data sets.

each of the $N^+ = 2, 4$ and 6 rotational levels. They are in agreement, within their uncertainties, with the more precise ab initio theoretical determinations [5, 10].

Table III. Summary of spin-rotation coupling constants γ_{SR} for the three lowest rotational levels of para-H₂⁺ and $\gamma_{\text{SR}}^{(0)}$ and $\gamma_{\text{SR}}^{(1)}$ obtained from Eq. 2.

γ_{SR}	Value (MHz)	Ref.
$\gamma_{\text{SR}}^{N^+=2}$	42.21(4)	This work
$\gamma_{\text{SR}}^{N^+=2}$	42.16352(15)	Theory [10]
$\gamma_{\text{SR}}^{N^+=4}$	41.26(8)	This work
$\gamma_{\text{SR}}^{N^+=4}$	41.2942	Theory [5]
$\gamma_{\text{SR}}^{N^+=6}$	40.04(8)	This work
$\gamma_{\text{SR}}^{(0)}$	42.53(9)	This work
$\gamma_{\text{SR}}^{(1)}$	-0.060(3)	This work

V. CONCLUSIONS

In this article, we have presented a study of the nf Rydberg series of H₂ converging on the low-lying $N^+ = 2, 4$ and 6 rotational levels of the $X^+ \ ^2\Sigma_g^+(v^+ = 0)$ vibronic ground state of para-H₂⁺. Using single-mode and frequency-comb-calibrated continuous-wave laser radiation, we have recorded spectra of Rydberg states over a broad range of principal quantum number n , from below 40 to 115. These spectra reveal, with full details, how the fine structure of the Rydberg states gradually evolves from a situation where the interactions determining the level patterns are the short-range electrostatic exchange interaction and the long-range electrostatic interactions between the Rydberg electron and the ion core, to a situation where the spin-rotation interaction in the ionic core determines the main fine-structure splittings.

In the former situation, the Rydberg states form two groups of levels of well-defined total electron spin ($S = 0$ or 1). Each group displays splittings characteristic of the long-range electrostatic interactions that couple the Rydberg-electron orbital angular momentum $\vec{\ell}$ to the

H_2^+ -ion-core rotational angular momentum \vec{N}^+ to form a nearly conserved total angular momentum \vec{N} . In the latter situation, the Rydberg electron is decoupled from the ion core so that the main splitting of the fine-structure pattern corresponds to the spin-rotation interval of the H_2^+ ion core.

The observed gradual uncoupling of the Rydberg electron with increasing n value was quantitatively analyzed in MQDT calculations using quantum defects derived from recent high-level ab initio calculations of low- n Rydberg states of H_2 . These calculations were used to extrapolate the Rydberg series to their limits and to determine, for the first time, the rotational and spin-rotational structures of the ground vibronic state of para- H_2^+ with sub-MHz accuracy.

Comparing the experimentally measured positions of several nf series with the positions calculated by MQDT revealed an overall excellent agreement, within the experimental uncertainties, but also significant discrepancies in the vicinity of low- n perturbing Rydberg states with a vibrationally excited H_2^+ ion core. These discrepancies could be attributed to the energy-reference ambiguity of standard MQDT and quantitatively accounted for using a simple empirical model involving two interacting channels. In future, a detailed analysis of these discrepan-

cies may serve as benchmarks for extensions of MQDT beyond the approximation of channel-independent reference electron energies.

The combination of precision Rydberg spectroscopy with MQDT is demonstrated to be a very attractive way to achieve a simultaneously global and precise description of molecular photoionization and to accurately determine the energies of a broad range of electronic, vibrational, and rotational levels of molecular ions, including their fine and hyperfine structures.

ACKNOWLEDGMENTS

We thank Dr. Christian Jungen, Orsay, for his invaluable assistance and discussions concerning all aspects of multichannel quantum-defect theory and also for allowing us to use his programs. We also thank Hansjürg Schmutz and Josef A. Agner for their technical assistance. M.B. acknowledges NWO for a VENI grant (VI.Veni.202.140). This work is supported financially by the Swiss National Science Foundation under the excellence grant No. 200020B-200478.

-
- [1] M. Puchalski, J. Komasa, P. Czachorowski, and K. Pachucki, Nonadiabatic QED correction to the dissociation energy of the hydrogen molecule, *Phys. Rev. Lett.* **122**, 103003 (2019).
- [2] M. Puchalski, J. Komasa, A. Spyszkiwicz, and K. Pachucki, Dissociation energy of molecular hydrogen isotopologues, *Phys. Rev. A* **100**, 020503 (2019).
- [3] V. I. Korobov, Leading-order relativistic and radiative corrections to the rovibrational spectrum of H_2^+ and HD^+ molecular ions, *Phys. Rev. A* **74**, 052506 (2006).
- [4] V. I. Korobov, Relativistic corrections of $m\alpha^6$ order to the rovibrational spectrum of H_2^+ and HD^+ molecular ions, *Phys. Rev. A* **77**, 022509 (2008).
- [5] V. I. Korobov, L. Hilico, and J.-Ph. Karr, Hyperfine structure in the hydrogen molecular ion, *Phys. Rev. A* **74**, 040502(R) (2006).
- [6] V. I. Korobov, L. Hilico, and J.-P. Karr, Theoretical transition frequencies beyond 0.1 ppb accuracy in H_2^+ , HD^+ , and antiprotonic helium, *Phys. Rev. A* **89**, 032511 (2014).
- [7] V. I. Korobov, L. Hilico, and J.-Ph. Karr, Fundamental transitions and ionization energies of the hydrogen molecular ions with few ppt uncertainty, *Phys. Rev. Lett.* **118**, 233001 (2017).
- [8] J. C. J. Koelemeij, Effect of correlated hyperfine theory errors in the determination of rotational and vibrational transition frequencies in HD^+ , *Mol. Phys.* **120** (2022).
- [9] J.-P. Karr and J. C. J. Koelemeij, Extraction of spin-averaged rovibrational transition frequencies in HD^+ for the determination of fundamental constants, *Mol. Phys.* **121** (2023).
- [10] M. Haidar, V. I. Korobov, L. Hilico, and J.-P. Karr, Higher-order corrections to spin-orbit and spin-spin tensor interactions in hydrogen molecular ions: Theory and application to H_2^+ , *Phys. Rev. A* **106**, 022816 (2022).
- [11] S. Patra, M. Germann, J.-P. Karr, M. Haidar, L. Hilico, V. I. Korobov, F. M. J. Cozijn, K. S. E. Eikema, W. Ubachs, and J. C. J. Koelemeij, Proton-electron mass ratio from laser spectroscopy of HD^+ at the part-per-trillion level, *Science* **369**, 1238 (2020).
- [12] S. Alighanbari, G. S. Giri, F. L. Constantin, V. I. Korobov, and S. Schiller, Precise test of quantum electrodynamics and determination of fundamental constants with HD^+ ions, *Nature* **581**, 152 (2020).
- [13] I. V. Kortunov, S. Alighanbari, M. G. Hansen, G. S. Giri, V. I. Korobov, and S. Schiller, Proton-electron mass ratio by high-resolution optical spectroscopy of ion ensembles in the resolved-carrier regime, *Nat. Phys.* **17**, 569 (2021).
- [14] I. V. Kortunov, S. Alighanbari, M. G. Hansen, G. S. Giri, V. I. Korobov, and S. Schiller, Author correction: Proton-electron mass ratio by high-resolution optical spectroscopy of ion ensembles in the resolved-carrier regime, *Nat. Phys.* **20**, 1034 (2024).
- [15] M. Germann, S. Patra, J.-Ph. Karr, L. Hilico, V. I. Korobov, E. J. Salumbides, K. S. E. Eikema, W. Ubachs, and J. C. J. Koelemeij, Three-body QED test and fifth-force constraint from vibrations and rotations of HD^+ , *Phys. Rev. Research* **3**, L022028 (2021).
- [16] C. Delaunay, J.-P. Karr, T. Kitahara, J. C. J. Koelemeij, Y. Soreq, and J. Zupan, Self-consistent extraction of spectroscopic bounds on light new physics, *Phys. Rev. Lett.* **130**, 121801 (2023).
- [17] M. R. Schenkel, S. Alighanbari, and S. Schiller, Laser spectroscopy of a rovibrational transition in the molecular hydrogen ion H_2^+ , *Nature Physics* **20**, 383 (2024).

- [18] S. Schiller and J.-P. Karr, Prospects for the determination of fundamental constants with beyond-state-of-the-art uncertainty using molecular hydrogen ion spectroscopy, *Phys. Rev. A* **109**, 042825 (2024).
- [19] M. J. Seaton, Quantum defect theory, *Rep. Prog. Phys.* **46**, 167 (1983).
- [20] U. Fano, Quantum defect theory of l uncoupling in H_2 as an example of channel-interaction treatment, *Phys. Rev. A* **2**, 353 (1970), see erratum in *Phys. Rev. A* **15**, 817 (1977).
- [21] G. Herzberg and Ch. Jungen, Rydberg series and ionization potential of the H_2 molecule, *J. Mol. Spectrosc.* **41**, 425 (1972).
- [22] Ch. H. Greene and Ch. Jungen, Molecular applications of quantum defect theory, *Adv. At. Mol. Phys.* **21**, 51 (1985).
- [23] Ch. Jungen, *Molecular Applications of Quantum Defect Theory* (Institute of Physics Publishing, Bristol and Philadelphia, 1996).
- [24] Ch. Jungen, Elements of quantum defect theory, in *Handbook of High-Resolution Spectroscopy*, Vol. 1, edited by M. Quack and F. Merkt (John Wiley & Sons, Chichester, 2011) pp. 471–510.
- [25] F. Merkt, S. Willitsch, and U. Hollenstein, High-resolution photoelectron spectroscopy, in *Handbook of High-Resolution Spectroscopy*, Vol. 3, edited by M. Quack and F. Merkt (John Wiley & Sons, Chichester, 2011) pp. 1617–1654.
- [26] O. Atabek, D. Dill, and Ch. Jungen, Quantum-defect theory of excited ${}^1\Pi_u^-$ levels of H_2 , *Phys. Rev. Lett.* **33**, 123 (1974).
- [27] Ch. Jungen and O. Atabek, Rovibronic interactions in the photoabsorption spectrum of molecular hydrogen and deuterium: An application of multichannel quantum defect methods, *J. Chem. Phys.* **66**, 5584 (1977).
- [28] N. Y. Du and Ch. H. Greene, Quantum defect analysis of HD photoionization, *J. Chem. Phys.* **85**, 5430 (1986).
- [29] Ch. Jungen, I. Dabrowski, G. Herzberg, and M. Vervloet, High orbital angular momentum states in H_2 and D_2 . III. Singlet-triplet splittings, energy levels, and ionization potentials, *J. Chem. Phys.* **93**, 2289 (1990).
- [30] Ch. Jungen, I. Dabrowski, G. Herzberg, and M. Vervloet, Observed wave numbers and identification of transitions of H_2 and D_2 , *Phys. Aux. Publ. Serv.* **93**, JCPSA (1990).
- [31] K. P. Huber and Ch. Jungen, High-resolution jet absorption study of nitrogen near 800 Å, *J. Chem. Phys.* **92**, 850 (1990).
- [32] K. P. Huber, Ch. Jungen, K. Yoshino, K. Ito, and G. Stark, The f Rydberg series in the absorption spectrum of N_2 , *J. Chem. Phys.* **100**, 7957 (1994).
- [33] Ch. Jungen and S. C. Ross, Unified quantum-defect-theory treatment of molecular ionization and dissociation, *Phys. Rev. A* **55**, R2503 (1997).
- [34] Ch. Jungen and S. T. Pratt, Vibrational autoionization in polyatomic molecules, *J. Chem. Phys.* **106**, 9529 (1997).
- [35] Ch. Jungen and G. Raseev, Spin-electronic-rotational frame transformation for photoionization and Rydberg spectra of diatomic molecules, *Phys. Rev. A* **57**, 2407 (1998).
- [36] A. Osterwalder, A. Wüest, F. Merkt, and Ch. Jungen, High-resolution millimeter wave spectroscopy and multichannel quantum defect theory of the hyperfine structure in high Rydberg states of molecular hydrogen H_2 , *J. Chem. Phys.* **121**, 11810 (2004).
- [37] J. J. Kay, S. L. Coy, B. M. Wong, Ch. Jungen, and R. W. Field, A quantum defect model for the s, p, d, and f Rydberg series of CaF, *J. Chem. Phys.* **134**, 114313 (2011).
- [38] D. Sprecher, J. Liu, T. Krähenmann, M. Schäfer, and F. Merkt, High-resolution spectroscopy and quantum-defect model for the *gerade* triplet np and nf Rydberg states of He_2 , *J. Chem. Phys.* **140**, 064304 (2014).
- [39] D. Sprecher, Ch. Jungen, and F. Merkt, Determination of the binding energies of the np Rydberg states of H_2 , HD, and D_2 from high-resolution spectroscopic data by multichannel quantum-defect theory, *J. Comp. Phys.* **140**, 104303 (2014).
- [40] M. Sommavilla, F. Merkt, J. Zs. Mezei, and Ch. Jungen, Absorption, autoionization, and predissociation in molecular hydrogen: High-resolution spectroscopy and multichannel quantum defect theory, *J. Chem. Phys.* **144**, 084303 (2016).
- [41] H. A. Cruse, Ch. Jungen, and F. Merkt, Hyperfine structure of the ground state of para- D_2^+ by high-resolution Rydberg-state spectroscopy and multichannel quantum defect theory, *Phys. Rev. A* **77**, 042502 (2008).
- [42] M. Beyer, N. Hölsch, J. Hussels, C.-F. Cheng, E. J. Salumbides, K. S. E. Eikema, W. Ubachs, Ch. Jungen, and F. Merkt, Determination of the interval between the ground states of para- and ortho- H_2 , *Phys. Rev. Lett.* **123**, 163002 (2019).
- [43] I. Doran, N. Hölsch, M. Beyer, and F. Merkt, Zero-Quantum-Defect Method and the Fundamental Vibrational Interval of H_2^+ , *Phys. Rev. Lett.* **132**, 073001 (2024).
- [44] M. Siłkowski, M. Zientkiewicz, and K. Pachucki, Accurate Born-Oppenheimer potentials for excited Σ^+ states of the hydrogen molecule, *Adv. Quantum Chem.* **83**, 255 (2021).
- [45] M. Siłkowski and K. Pachucki, Born–Oppenheimer potentials for Π , Δ , and Φ states of the hydrogen molecule, *Mol. Phys.* **120** (2022).
- [46] M. Siłkowski, *Accurate calculations of binding energies of the ground and excited states of the hydrogen molecule*, Ph.D. thesis, University of Warsaw, Warsaw, Poland (2023).
- [47] M. Siłkowski, M. Beyer, and K. Pachucki, unpublished, (2024).
- [48] Ch. H. Greene and Ch. Jungen, Vibrational frame transformation for electron-molecule scattering, *Phys. Rev. Lett.* **55**, 1066 (1985).
- [49] H. Gao and Ch. H. Greene, Alternative vibrational frame transformation for electron-molecule scattering, *Phys. Rev. A* **42**, 6946 (1990).
- [50] D. Hvizdoš, C. H. Greene, and R. Čurík, Backpropagated frame transformation theory: A reformulation, *Phys. Rev. A* **101**, 012709 (2020).
- [51] C. Haase, M. Beyer, Ch. Jungen, and F. Merkt, The fundamental rotational interval of para- H_2^+ by MQDT-assisted Rydberg spectroscopy of H_2 , *J. Chem. Phys.* **142**, 064310 (2015).
- [52] M. Beyer, *Precision spectroscopy and dynamics of molecular hydrogen and its ion*, Ph.D. thesis, Eidgenössische Technische Hochschule, Zürich, Switzerland (2018), Diss. ETH Nr. 25199.
- [53] K. B. Jefferts, Hyperfine structure in the molecular ion H_2^+ , *Phys. Rev. Lett.* **23**, 1476 (1969).
- [54] M. Kristensen and N. Bjerre, Fine structure of the lowest triplet states in He_2 , *J. Chem. Phys.* **93**, 983 (1990).

- [55] P. Jansen, L. Semeria, and F. Merkt, Fundamental vibration frequency and rotational structure of the first excited vibrational level of the molecular helium ion (He_2^+), *J. Chem. Phys.* **149**, 154302 (2018).
- [56] N. Hölsch, M. Beyer, and F. Merkt, Nonadiabatic effects on the positions and lifetimes of the low-lying rovibrational levels of the GK $^1\Sigma_g^+$ and H $^1\Sigma_g^+$ states of H_2 , *Phys. Chem. Chem. Phys.* **20**, 26837 (2018).
- [57] M. Beyer, N. Hölsch, J. A. Agner, J. Deiglmayr, H. Schmutz, and F. Merkt, Metrology of high- n Rydberg states of molecular hydrogen with $\Delta\nu/\nu = 2 \times 10^{-10}$ accuracy, *Phys. Rev. A* **97**, 012501 (2018).
- [58] A. Osterwalder and F. Merkt, Using high Rydberg states as electric field sensors, *Phys. Rev. Lett.* **82**, 1831 (1999).
- [59] H. J. Wörner, S. Mollet, Ch. Jungen, and F. Merkt, Role of spins in molecular photoionization: Spectroscopy and dynamics of autoionizing Rydberg states of ortho- H_2 , *Phys. Rev. A* **75**, 062511 (2007).
- [60] N. Hölsch, M. Beyer, E. J. Salumbides, K. S. E. Eikema, W. Ubachs, Ch. Jungen, and F. Merkt, Benchmarking theory with an improved measurement of the ionization and dissociation energies of H_2 , *Phys. Rev. Lett.* **122**, 103002 (2019).
- [61] S. Ross and Ch. Jungen, Quantum-defect theory of double-minimum states in H_2 , *Phys. Rev. Lett.* **59**, 1297 (1987).
- [62] S. C. Ross and Ch. Jungen, Multichannel quantum-defect theory of double minimum $^1\Sigma_g^+$ states in H_2 . I. Potential-energy curves, *Phys. Rev. A* **49**, 4353 (1994).
- [63] S. C. Ross and Ch. Jungen, Multichannel quantum-defect theory of double minimum $^1\Sigma_g^+$ states in H_2 . II. Vibronic-energy levels, *Phys. Rev. A* **49**, 4364 (1994).
- [64] S. C. Ross and Ch. Jungen, Multichannel quantum-defect theory of $n=2$ and 3 gerade states in H_2 : Rovibronic energy levels, *Phys. Rev. A* **50**, 4618 (1994).
- [65] F. S. Ham, The quantum defect method, *Solid State Phys.* **1**, 127 (1955).
- [66] C. Jungen, The fine and hyperfine structures of the low- n $^3\Pi_u$ Rydberg states of H_2 revisited, *Mol. Phys.* **121** (2023).

I. SUPPLEMENTAL MATERIAL

This supplemental material provides information on

a) the energy-level structure of $nf4(J = 1)$ and $nf6(J = 3)$ Rydberg states of H_2 determined in MQDT calculations including electron spins, as described for $nf2(J=1)$ Rydberg states in the article (Figs. S1 and S2);

b) the measured positions of the nf Rydberg states of H_2 and their binding energies determined experimentally and by MQDT (before and after correcting with an empirical two-channel interaction model) using the fitted values of the spin-rotation coupling constants and of the $X^+(0, 2) - GK(0, 0)$, $X^+(0, 4) - GK(0, 2)$ and $X^+(0, 6) - I^+(0, 4)$ intervals (Tables S1, S2, S3).

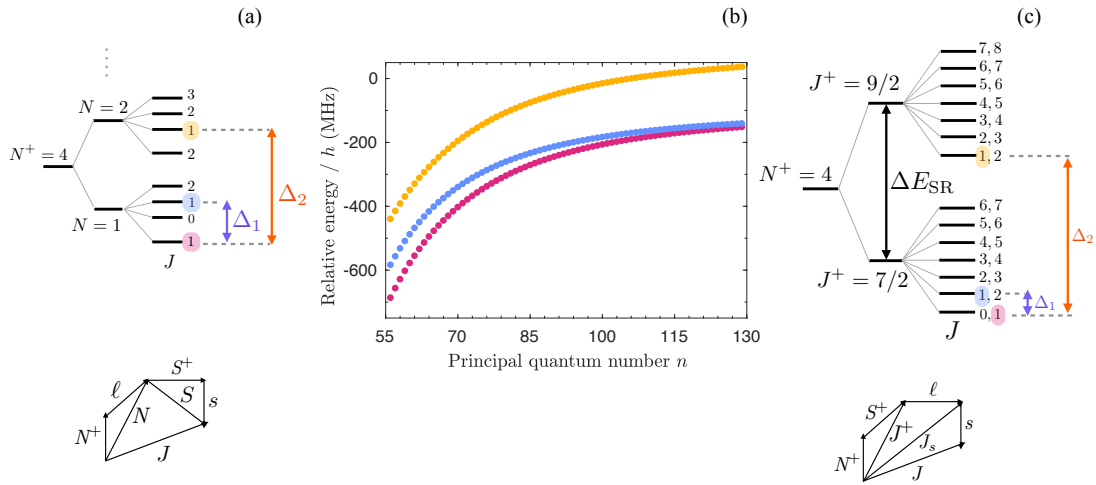


FIG. S1. Positions of the $nf4(J = 1)$ Rydberg states of H_2 , obtained in an MQDT calculation including electron spins, relative to the zero-quantum-defect positions $-cR_{H_2}/n^2$ (panel (b)).

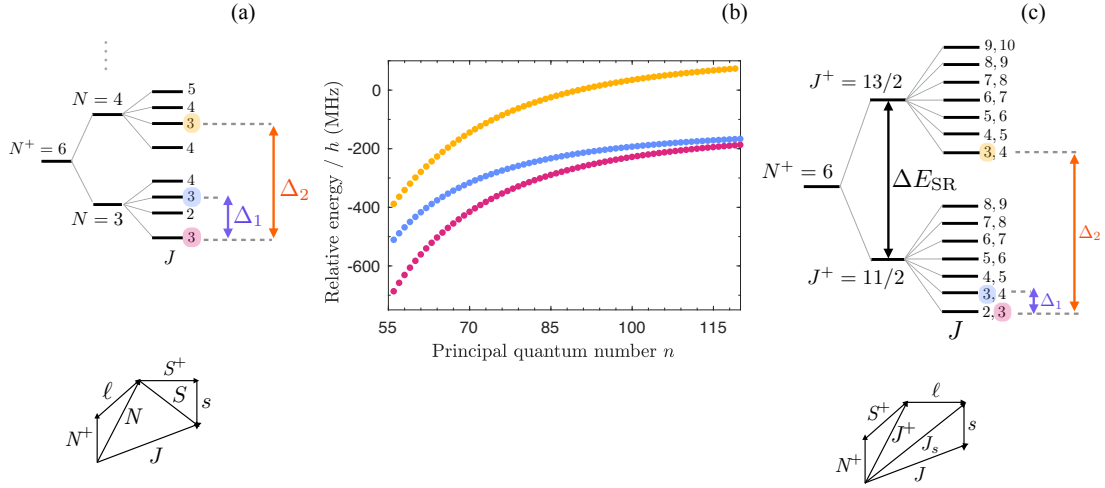


FIG. S2. Positions of the $nf6(J = 3)$ Rydberg states of H_2 , obtained in an MQDT calculation including electron spins, relative to the zero-quantum-defect positions $-cR_{\text{H}_2}/n^2$ (panel (b)).

TABLE S1: Experimental positions (in wavenumber units cm^{-1}) of the measured fine-structure components of the $n\ell(J=1)$ Rydberg states of H_2 relative to the GK(0,0) state, their statistical uncertainties (in MHz), their binding energies determined using the measured positions and the fitted $\gamma_{\text{SR}}^{N^+=2}$ and $X^+(0,2)$ –GK(0,0) interval, their binding energies calculated by MQDT, their binding energies calculated by MQDT after correcting with a two-channel interaction model, the deviation between experiment and MQDT calculations, and the deviation between experiment and MQDT after correcting with a two-channel interaction model. The states are labelled by the principal quantum number n and by the letter A, B or C to denote the different fine-structure components of $J=1$ in the order of increasing energy at each value of n .

n (Label)	$\tilde{\nu}_{\text{obs}}$ (cm^{-1})	σ (MHz)	$E_{\text{bind}}^{\text{obs}} / hc$ (cm^{-1})	$E_{\text{bind}}^{\text{MQDT}} / hc$ (cm^{-1})	$E_{\text{bind}}^{\text{corr}} / hc$ (cm^{-1})	$\nu_{\text{obs}} - \nu_{\text{MQDT}}$ (MHz)	$\nu_{\text{obs}} - \nu_{\text{corr}}$ (MHz)
36(A)	12 878.152 5044	0.523	−84.724 104 5	−84.723 857 4	−84.723 538 4	−7.409	−16.972
36(B)	12 878.154 913 1	0.616	−84.721 695 8	−84.721 747 8	−84.721 428 8	1.557	−8.004
37(A)	12 882.671 851 9	0.327	−80.204 757 0	−80.205 218 8	−80.204 837 2	13.843	2.404
37(B)	12 882.673 956 1	0.269	−80.202 652 8	−80.203 099 2	−80.202 717 6	13.381	1.943
38(A)	12 886.837 940 7	0.429	−76.038 668 2	−76.039 174 5	−76.038 670 4	15.177	0.063
38(B)	12 886.840 072 8	0.448	−76.036 536 1	−76.037 048 6	−76.036 544 5	15.363	0.250
39(A)	12 890.685 989 5	0.511	−72.190 619 5	−72.191 446 8	−72.190 619 0	24.803	−0.014
39(B)	12 890.688 110 6	0.381	−72.188 498 4	−72.189 326 9	−72.188 499 1	24.839	0.024
40(A)	12 894.227 923 9	0.261	−68.648 685 1	−68.651 506 9	−68.647 892 3	84.596	−23.765
40(B)	12 894.230 707 0	0.462	−68.645 902 0	−68.649 359 1	−68.645 744 7	103.642	−4.714
41(A)	12 897.574 332 0	0.367	−65.302 277 0	−65.301 074 7	−65.302 272 6	−36.043	−0.132
41(B)	12 897.576 588 4	0.287	−65.300 020 6	−65.298 823 3	−65.300 021 1	−35.893	0.016
44(A)	12 906.171 907 6	0.164	−56.704 701 4	−56.704 510 2	−56.704 691 8	−5.731	−0.286
44(B)	12 906.174 130 8	0.159	−56.702 478 2	−56.702 293 3	−56.702 474 9	−5.542	−0.097

46(A)	12 910.996 478 3	0.107	-51.880 130 7	-51.880 029 8	-51.880 128 6	-3.024	-0.062
46(B)	12 910.998 730 1	0.090	-51.877 878 9	-51.877 788 3	-51.877 887 1	-2.716	0.246
48(A)	12 915.230 709 4	0.075	-47.645 899 6	-47.645 833 8	-47.645 894 4	-1.972	-0.154
48(B)	12 915.232 987 2	0.094	-47.643 621 8	-47.643 567 3	-47.643 627 9	-1.633	0.185
50(A)	12 918.967 018 8	0.076	-43.909 590 2	-43.909 547 8	-43.909 587 1	-1.271	-0.091
50(B)	12 918.969 312 1	0.095	-43.907 296 9	-43.907 255 4	-43.907 294 7	-1.244	-0.064
52(A)	12 922.280 477 9	0.091	-40.596 131 1	-40.596 098 1	-40.596 124 2	-0.989	-0.206
52(B)	12 922.282 801 3	0.087	-40.593 807 7	-40.593 778 7	-40.593 804 8	-0.869	-0.087
54(A)	12 925.232 566 4	0.093	-37.644 042 6	-37.644 023 5	-37.644 040 8	-0.572	-0.055
54(B)	12 925.234 918 7	0.101	-37.641 690 3	-37.641 675 9	-37.641 693 2	-0.431	0.086
57(A)	12 929.091 601 3	0.079	-33.785 007 7	-33.784 995 7	-33.785 004 4	-0.360	-0.100
57(B)	12 929.094 000 6	0.092	-33.782 608 4	-33.782 603 1	-33.782 611 8	-0.159	0.101
58(A)	12 930.246 789 4	0.100	-32.629 819 6	-32.629 814 0	-32.629 820 6	-0.168	0.030
58(B)	12 930.249 200 1	0.105	-32.627 408 9	-32.627 405 4	-32.627 412 0	-0.105	0.093
60(A)	12 932.386 225 2	0.198	-30.490 383 8	-30.490 374 1	-30.490 377 3	-0.291	-0.194
60(B)	12 932.388 681 0	0.170	-30.487 928 0	-30.487 930 0	-30.487 933 2	0.060	0.157
61(A)	12 933.377 873 3	0.240	-29.498 735 7	-29.498 747 2	-29.498 749 1	0.345	0.401
61(B)	12 933.380 336 4	0.326	-29.496 272 6	-29.496 280 3	-29.496 282 2	0.231	0.287
62(A)	12 934.321 690 5	0.177	-28.554 918 5	-28.554 917 7	-28.554 918 4	-0.024	-0.004
62(B)	12 934.324 198 4	0.217	-28.552 410 6	-28.552 409 9	-28.552 410 6	-0.021	-0.001
63(A)	12 935.221 799 4	0.178	-27.654 809 6	-27.654 807 0	-27.654 806 6	-0.078	-0.090

63(B)	12 935.224 182 8	0.220	-27.652 426 2	-27.652 424 9	-27.652 424 5	-0.039	-0.051
64(A)	12 936.079 208 0	0.097	-26.797 401 0	-26.797 399 9	-26.797 398 5	-0.033	-0.073
64(B)	12 936.081 676 6	0.153	-26.794 932 4	-26.794 933 2	-26.794 931 8	0.024	-0.016
65(A)	12 936.897 511 0	0.185	-25.979 098 0	-25.979 114 1	-25.979 111 9	0.483	0.417
65(B)	12 936.900 001 9	0.206	-25.976 607 1	-25.976 620 5	-25.976 618 3	0.402	0.336
66(A)	12 937.678 879 1	0.155	-25.197 729 9	-25.197 727 2	-25.197 724 3	-0.081	-0.169
66(B)	12 937.681 408 3	0.169	-25.195 200 7	-25.195 213 3	-25.195 210 4	0.378	0.290
68(A)	12 939.139 492 5	0.129	-23.737 116 5	-23.737 108 9	-23.737 104 7	-0.228	-0.354
68(B)	12 939.142 049 3	0.190	-23.734 559 7	-23.734 559 2	-23.734 555 0	-0.015	-0.142
70(A)	12 940.476 701 8	0.142	-22.399 907 2	-22.399 909 1	-22.399 903 8	0.057	-0.101
70(B)	12 940.479 287 8	0.127	-22.397 321 2	-22.397 325 6	-22.397 320 3	0.132	-0.026
74(A)	12 942.833 114 7	0.236	-20.043 494 3	-20.043 488 7	-20.043 481 9	-0.168	-0.373
74(B)	12 942.835 769 7	0.330	-20.040 839 3	-20.040 839 5	-20.040 832 7	0.006	-0.199
77(A)	12 944.364 657 1	0.228	-18.511 951 9	-18.511 943 5	-18.511 935 8	-0.252	-0.483
77(B)	12 944.367 362 9	0.308	-18.509 246 1	-18.509 246 2	-18.509 238 5	0.003	-0.228
80(A)	12 945.727 123 3	0.259	-17.149 485 7	-17.149 478 7	-17.149 470 3	-0.210	-0.461
80(B)	12 945.729 873 4	0.182	-17.146 735 6	-17.146 734 4	-17.146 726 0	-0.036	-0.287
90(A)	12 949.326 519 0	0.138	-13.550 090 0	-13.550 080 6	-13.550 070 8	-0.282	-0.575
90(B)	12 949.329 399 9	0.175	-13.547 209 1	-13.547 191 8	-13.547 182 0	-0.519	-0.812
100(A)	12 951.900 979 7	0.123	-10.975 629 3	-10.975 611 9	-10.975 601 4	-0.522	-0.837
100(B)	12 951.903 992 9	0.120	-10.972 616 1	-10.972 600 9	-10.972 590 4	-0.456	-0.771

105(A)	12 952.921 317 7	0.211	-9.955 291 3	-9.955 266 1	-9.955 255 4	-0.756	-1.078
105(B)	12 952.924 384 8	0.293	-9.952 224 2	-9.952 202 8	-9.952 192 1	-0.642	-0.964
110(A)	12 953.805 640 4	0.312	-9.070 968 6	-9.070 889 5	-9.070 878 6	-2.372	-2.699
110(B)	12 953.808 753 7	0.290	-9.067 855 3	-9.067 779 5	-9.067 768 6	-2.273	-2.600
115(A)	12 954.577 244 8	0.253	-8.299 364 2	-8.299 354 0	-8.299 342 9	-0.306	-0.638
115(B)	12 954.580 355 1	0.401	-8.296 253 9	-8.296 202 6	-8.296 191 5	-1.538	-1.870

TABLE S2: Experimental positions (in wavenumber units cm^{-1}) of the measured fine-structure components of the $nf4(J=1)$ Rydberg states of H_2 relative to the GK(0,2) state, their statistical uncertainties (in MHz), their binding energies determined using the measured positions and the fitted $\gamma_{\text{SR}}^{N^+=4}$ and $X^+(0,4)$ -GK(0,2) interval, their binding energies calculated by MQDT, their binding energies calculated by MQDT after correcting with a two-channel interaction model, the deviation between experiment and MQDT calculations, and the deviation between experiment and MQDT after correcting with a two-channel interaction model. The states are labelled by the principal quantum number n and by the letter A, B or C to denote the different fine-structure components of $J=1$ in the order of increasing energy at each value of n .

n (Label)	$\tilde{\nu}_{\text{obs}}$ (cm^{-1})	σ (MHz)	$E_{\text{bind}}^{\text{obs}} / hc$ (cm^{-1})	$E_{\text{bind}}^{\text{MQDT}} / hc$ (cm^{-1})	$E_{\text{bind}}^{\text{corr}} / hc$ (cm^{-1})	$\nu_{\text{obs}} - \nu_{\text{MQDT}}$ (MHz)	$\nu_{\text{obs}} - \nu_{\text{corr}}$ (MHz)
33(A)	13 198.368 193 6	0.737	-100.844 879 6	-100.845 411 8	-100.844 854 4	15.954	-0.757
33(B)	13 198.373 337 9	0.445	-100.839 735 3	-100.840 320 2	-100.839 762 8	17.534	0.824
34(A)	13 204.211 198 0	0.461	-95.001 875 2	-95.002 825 1	-95.001 888 1	28.476	0.386
34(B)	13 204.216 385 8	0.342	-94.996 687 4	-94.997 718 3	-94.996 781 4	30.904	2.816
36(A)	13 214.493 183 9	1.062	-84.719 889 3	-84.718 918 9	-84.719 906 9	-29.093	0.527
36(B)	13 214.498 203 3	0.489	-84.714 869 9	-84.713 895 1	-84.714 883 0	-29.225	0.393

39(A)	13 227.025 080 8	0.261	-72.187 992 4	-72.187 779 5	-72.187 935 5	-6.385	-1.707
39(B)	13 227.029 902 3	0.212	-72.183 170 9	-72.182 990 4	-72.183 146 4	-5.413	-0.736
42(A)	13 236.971 877 7	0.296	-62.241 195 5	-62.241 087 7	-62.241 147 7	-3.234	-1.434
42(B)	13 236.976 542 1	0.282	-62.236 531 1	-62.236 452 2	-62.236 512 2	-2.368	-0.568
44(A)	13 242.503 038 3	0.574	-56.710 035 0	-56.709 942 6	-56.709 977 4	-2.769	-1.727
44(B)	13 242.507 589 6	0.345	-56.705 483 7	-56.705 428 7	-56.705 463 4	-1.648	-0.606
45(A)	13 244.996 095 8	0.414	-54.216 977 5	-54.216 846 2	-54.216 872 7	-3.936	-3.140
45(B)	13 245.000 618 7	0.254	-54.212 454 6	-54.212 399 6	-54.212 426 1	-1.648	-0.853
46(A)	13 247.328 547 4	0.414	-51.884 525 9	-51.884 610 9	-51.884 631 0	2.549	3.151
46(B)	13 247.332 846 0	0.532	-51.880 227 3	-51.880 236 3	-51.880 256 4	0.270	0.873
47(A)	13 249.513 376 2	0.270	-49.699 697 1	-49.699 692 2	-49.699 707 1	-0.146	0.302
47(B)	13 249.517 664 4	0.244	-49.695 408 9	-49.695 394 0	-49.695 408 9	-0.446	0.002
48(A)	13 251.563 094 9	0.692	-47.649 978 4	-47.649 940 4	-47.649 951 2	-1.139	-0.814
48(B)	13 251.567 381 0	0.530	-47.645 692 3	-47.645 723 3	-47.645 734 1	0.930	1.254
48(C)	13 251.573 778 3	0.840	-47.639 295 0	-47.639 321 9	-47.639 332 7	0.807	1.131
50(A)	13 255.299 723 8	0.292	-43.913 349 5	-43.913 328 1	-43.913 332 7	-0.641	-0.502
50(B)	13 255.303 770 1	0.284	-43.909 303 2	-43.909 286 8	-43.909 291 4	-0.491	-0.352
50(C)	13 255.309 559 8	0.717	-43.903 513 5	-43.903 517 6	-43.903 522 2	0.123	0.262
51(A)	13 257.005 306 2	0.568	-42.207 767 1	-42.207 740 0	-42.207 742 3	-0.812	-0.743
51(B)	13 257.009 281 9	0.453	-42.203 791 4	-42.203 792 8	-42.203 795 1	0.042	0.112
51(C)	13 257.014 810 9	0.770	-42.198 262 4	-42.198 272 4	-42.198 274 7	0.300	0.369
52(A)	13 258.613 443 8	0.353	-40.599 629 5	-40.599 628 6	-40.599 628 9	-0.027	-0.016

52(B)	13 258.617 297 6	0.253	-40.595 775 7	-40.595 779 1	-40.595 779 4	0.102	0.113
52(C)	13 258.622 621 5	0.360	-40.590 451 8	-40.590 468 1	-40.590 468 4	0.489	0.499
55(A)	13 262.922 521 7	0.365	-36.290 551 6	-36.290 539 9	-36.290 535 9	-0.351	-0.469
55(B)	13 262.926 066 2	0.349	-36.287 007 1	-36.286 999 6	-36.286 995 6	-0.225	-0.343
55(C)	13 262.930 965 1	0.643	-36.282 108 2	-36.282 117 9	-36.282 113 9	0.291	0.172
58(A)	13 266.580 261 6	0.333	-32.632 811 7	-32.632 810 4	-32.632 803 7	-0.039	-0.240
58(B)	13 266.583 487 1	0.348	-32.629 586 2	-32.629 589 9	-32.629 583 2	0.111	-0.090
58(C)	13 266.588 179 7	0.534	-32.624 893 6	-32.624 913 1	-32.624 906 4	0.585	0.384
60(A)	13 268.719 868 6	0.423	-30.493 204 7	-30.493 213 6	-30.493 205 6	0.267	0.027
60(B)	13 268.722 874 5	0.494	-30.490 198 8	-30.490 204 0	-30.490 196 0	0.156	-0.084
60(C)	13 268.727 493 7	0.532	-30.485 579 6	-30.485 579 3	-30.485 571 3	-0.009	-0.249
64(A)	13 272.412 890 1	0.740	-26.800 183 2	-26.800 192 3	-26.800 182 5	0.273	-0.021
64(B)	13 272.415 493 5	0.458	-26.797 579 8	-26.797 581 6	-26.797 571 8	0.054	-0.240
64(C)	13 272.420 146 5	0.662	-26.792 926 8	-26.792 939 5	-26.792 929 7	0.381	0.086
67(A)	13 274.759 445 6	0.736	-24.453 627 7	-24.453 650 6	-24.453 639 9	0.686	0.365
67(B)	13 274.761 771 9	1.193	-24.451 301 4	-24.451 310 8	-24.451 300 1	0.282	-0.040
67(C)	13 274.766 496 1	0.457	-24.446 577 2	-24.446 596 7	-24.446 586 0	0.584	0.263
70(A)	13 276.810 737 5	0.415	-22.402 335 8	-22.402 355 9	-22.402 344 5	0.602	0.262
70(B)	13 276.812 853 3	1.345	-22.400 220 0	-22.400 259 6	-22.400 248 2	1.187	0.846
70(C)	13 276.817 641 1	0.299	-22.395 432 2	-22.395 451 4	-22.395 440 0	0.575	0.235
80(A)	13 282.061 468 2	0.132	-17.151 605 1	-17.151 583 1	-17.151 570 5	-0.660	-1.036
80(B)	13 282.062 936 9	0.144	-17.150 136 4	-17.150 115 7	-17.150 103 1	-0.621	-0.997

80(C)	13 282.068 060 3	0.123	-17.145 013 0	-17.144 974 8	-17.144 962 2	-1.146	-1.522
90(A)	13 285.661 120 3	0.534	-13.551 953 0	-13.551 936 1	-13.551 923 0	-0.507	-0.899
90(B)	13 285.662 171 2	0.468	-13.550 902 1	-13.550 882 1	-13.550 869 0	-0.600	-0.991
90(C)	13 285.667 541 5	0.225	-13.545 531 8	-13.545 474 1	-13.545 461 0	-1.730	-2.122
100(A)	13 288.235 774 2	0.176	-10.977 299 1	-10.977 279 8	-10.977 266 5	-0.579	-0.978
100(B)	13 288.236 551 5	0.367	-10.976 521 8	-10.976 501 4	-10.976 488 1	-0.612	-1.011
100(C)	13 288.242 153 6	0.152	-10.970 919 7	-10.970 900 2	-10.970 886 9	-0.585	-0.984
110(A)	13 290.140 625 2	0.340	-9.072 448 1	-9.072 415 0	-9.072 401 6	-0.993	-1.395
110(B)	13 290.141 208 0	0.576	-9.071 865 3	-9.071 825 5	-9.071 812 1	-1.194	-1.596
110(C)	13 290.146 962 5	0.230	-9.066 110 8	-9.066 086 4	-9.066 073 0	-0.732	-1.134

TABLE S3: Experimental positions (in wavenumber units cm^{-1}) of the measured fine-structure components of the $nf6(J=3)$ Rydberg states of H_2 relative to the $\text{I}^+(0,4)$ state, their statistical uncertainties (in MHz), their binding energies determined using the measured positions and the fitted $\gamma_{\text{SR}}^{N^+=6}$ and $\text{X}^+(0,6) - \text{I}^+(0,4)$ interval, their binding energies calculated by MQDT, their binding energies calculated by MQDT after correcting with a two-channel interaction model, the deviation between experiment and MQDT calculations, and the deviation between experiment and MQDT after correcting with a two-channel interaction model. The states are labelled by the principal quantum number n and by the letter A, B or C to denote the different fine-structure components of $J=3$ in the order of increasing energy at each value of n .

$n(\text{Label})$	$\tilde{\nu}_{\text{obs}} (\text{cm}^{-1})$	$\sigma (\text{MHz})$	$E_{\text{bind}}^{\text{obs}} / hc (\text{cm}^{-1})$	$E_{\text{bind}}^{\text{MQDT}} / hc (\text{cm}^{-1})$	$E_{\text{bind}}^{\text{corr}} / hc (\text{cm}^{-1})$	$\nu_{\text{obs}} - \nu_{\text{MQDT}} (\text{MHz})$	$\nu_{\text{obs}} - \nu_{\text{corr}} (\text{MHz})$
28(A)	12 765.093 829 9	0.736	-140.090 312 0	-140.090 689 2	-140.090 074 8	11.307	-7.111
28(B)	12 765.102 112 1	0.613	-140.082 029 8	-140.082 486 2	-140.081 871 9	13.681	-4.735

29(A)	12 774.589 448 0	0.770	-130.594 693 9	-130.595 462 6	-130.594 419 8	23.044	-8.219
29(B)	12 774.597 695 4	0.638	-130.586 446 5	-130.587 275 6	-130.586 232 9	24.854	-6.405
31(A)	12 790.917 370 9	0.843	-114.266 771 1	-114.265 832 3	-114.266 689 8	-28.143	-2.436
31(B)	12 790.925 553 9	0.703	-114.258 588 1	-114.257 708 0	-114.258 565 4	-26.383	-0.679
33(A)	12 804.349 271 8	0.754	-100.834 870 2	-100.834 558 4	-100.834 767 0	-9.347	-3.094
33(B)	12 804.357 388 3	0.588	-100.826 753 7	-100.826 478 9	-100.826 687 4	-8.237	-1.986
36(A)	12 820.459 641 9	0.882	-84.724 500 1	-84.724 342 1	-84.724 408 6	-4.736	-2.742
36(B)	12 820.467 665 8	0.624	-84.716 476 2	-84.716 336 6	-84.716 403 1	-4.185	-2.190
40(A)	12 836.561 866 2	0.999	-68.622 275 8	-68.622 183 6	-68.622 204 1	-2.764	-2.150
40(B)	12 836.569 742 8	0.890	-68.614 399 2	-68.614 314 3	-68.614 334 8	-2.545	-1.932
43(A)	12 845.805 454 4	1.292	-59.378 687 6	-59.378 608 5	-59.378 616 7	-2.371	-2.125
43(B)	12 845.813 251 8	0.983	-59.370 890 2	-59.370 890 4	-59.370 898 6	0.006	0.252
46(A)	12 853.299 748 0	1.388	-51.884 393 9	-51.884 383 5	-51.884 385 7	-0.312	-0.247
46(B)	12 853.307 181 6	0.986	-51.876 960 3	-51.876 889 1	-51.876 891 3	-2.135	-2.070
49(A)	12 859.459 748 2	1.074	-45.724 393 7	-45.724 412 2	-45.724 411 2	0.554	0.523
49(B)	12 859.466 877 4	1.079	-45.717 264 5	-45.717 254 2	-45.717 253 2	-0.309	-0.341
52(A)	12 864.584 319 7	1.057	-40.599 822 2	-40.599 789 7	-40.599 786 9	-0.975	-1.060
52(B)	12 864.591 028 2	1.331	-40.593 113 7	-40.593 112 3	-40.593 109 5	-0.043	-0.127
52(C)	12 864.595 232 7	1.619	-40.588 909 2	-40.588 894 0	-40.588 891 2	-0.456	-0.541
55(A)	12 868.893 320 7	0.666	-36.290 821 2	-36.290 854 2	-36.290 850 4	0.989	0.873
55(B)	12 868.899 286 6	0.990	-36.284 855 3	-36.284 780 3	-36.284 776 5	-2.249	-2.364
55(C)	12 868.903 441 0	0.945	-36.280 700 9	-36.280 728 6	-36.280 724 8	0.830	0.714

58(A)	12 872.550 985 2	1.067	-32.633 156 7	-32.633 252 3	-32.633 247 9	2.865	2.732
58(B)	12 872.556 432 0	1.956	-32.627 709 9	-32.627 828 2	-32.627 823 8	3.546	3.413
58(C)	12 872.560 573 6	1.238	-32.623 568 3	-32.623 581 9	-32.623 577 5	0.407	0.274
61(A)	12 875.682 197 4	0.798	-29.501 944 5	-29.502 032 2	-29.502 027 4	2.628	2.486
61(B)	12 875.686 921 2	2.190	-29.497 220 7	-29.497 233 1	-29.497 228 3	0.371	0.228
61(C)	12 875.691 579 8	0.822	-29.492 562 1	-29.492 635 7	-29.492 630 9	2.206	2.063
65(A)	12 879.201 621 1	0.969	-25.982 520 8	-25.982 479 5	-25.982 474 5	-1.239	-1.388
65(B)	12 879.205 652 0	2.746	-25.978 489 9	-25.978 418 5	-25.978 413 5	-2.141	-2.290
65(C)	12 879.210 744 1	1.423	-25.973 397 8	-25.973 300 3	-25.973 295 3	-2.924	-3.073
70(A)	12 882.781 119 1	1.199	-22.403 022 8	-22.403 130 0	-22.403 125 0	3.213	3.062
70(B)	12 882.784 417 9	2.572	-22.399 724 0	-22.399 822 5	-22.399 817 5	2.952	2.801
70(C)	12 882.789 977 4	1.296	-22.394 164 5	-22.394 105 2	-22.394 100 2	-1.779	-1.930
80(A)	12 888.031 603 3	0.417	-17.152 538 6	-17.152 506 7	-17.152 501 8	-0.958	-1.106
80(B)	12 888.033 817 0	0.357	-17.150 324 9	-17.150 252 9	-17.150 248 0	-2.160	-2.308
80(C)	12 888.040 484 1	0.423	-17.143 657 8	-17.143 632 7	-17.143 627 8	-0.754	-0.902
90(A)	12 891.631 177 4	0.671	-13.552 964 5	-13.552 951 1	-13.552 946 3	-0.403	-0.547
90(C)	12 891.639 953 9	0.618	-13.544 188 0	-13.544 147 1	-13.544 142 3	-1.227	-1.371
95(A)	12 893.020 024 8	0.878	-12.164 117 1	-12.164 101 6	-12.164 096 9	-0.466	-0.608
95(C)	12 893.028 793 1	0.606	-12.155 348 8	-12.155 319 3	-12.155 314 6	-0.886	-1.027
100(A)	12 894.205 758 5	0.690	-10.978 383 4	-10.978 353 7	-10.978 349 0	-0.892	-1.031
100(C)	12 894.214 535 5	0.399	-10.969 606 4	-10.969 588 1	-10.969 583 4	-0.550	-0.690